Journal of Nanobiotechnology

RESEARCH

Open Access

Injectable hydrogels with ROS-triggered drug release enable the co-delivery of antibacterial agent and anti-inflammatory nanoparticle for periodontitis treatment

Yujing Zhu[1,2], Ziliang Xiu[1,2], Xiaoxi Jiang[3], Huifang Zhang[1], Xiaofeng Li[1,2], Yunru Feng[1,2], Bojiang Li[1], Rui Cai[1,4*], Chunhui Li[1,2,4*] and Gang Tao[1,4*]

Abstract

Periodontitis, a chronic inflammatory disease caused by bacteria, is characterized by localized reactive oxygen species (ROS) accumulation, leading to an inflammatory response, which in turn leads to the destruction of periodontal supporting tissues. Therefore, antibacterial, scavenging ROS, reducing the inflammatory response, regulating periodontal microenvironment, and alleviating alveolar bone resorption are effective methods to treat periodontitis. In this study, we developed a ROS-responsive injectable hydrogel by modifying hyaluronic acid with 3-amino phenylboronic acid (PBA) and reacting it with poly(vinyl alcohol) (PVA) to form a borate bond. In addition, the ROS-responsive hydrogel encapsulated the antibacterial agent minocycline hydrochloride (MH) and Fe-Quercetin anti-inflammatory nanoparticles (Fe-Que NPs) for on-demand drug release in response to the periodontitis microenvironment. This hydrogel (HP-PVA@MH/Fe-Que) exhibited highly effective antibacterial properties. Moreover, by modulating the Nrf2/NF-κB pathway, it effectively eliminated ROS and promoted macrophage polarization to the M2 phenotype, reducing inflammation and enhancing the osteogenic differentiation potential of human periodontal ligament stem cells (hPDLSCs) in the periodontal microenvironment. Animal studies showed that HP-PVA@MH/Fe-Que significantly reduced alveolar bone loss and enhanced osteogenic factor expression by killing bacteria and inhibiting inflammation. Thus, HP-PVA@MH/Fe-Que hydrogel had efficient antibacterial, ROS-scavenging, anti-inflammatory, and alveolar bone resorption-alleviation abilities, showing excellent application potential for periodontitis healing.

*Correspondence:
Rui Cai
cairui@swmu.edu.cn
Chunhui Li
lch10221022@163.com
Gang Tao
taogang@swmu.edu.cn

Full list of author information is available at the end of the article

Graphical abstract

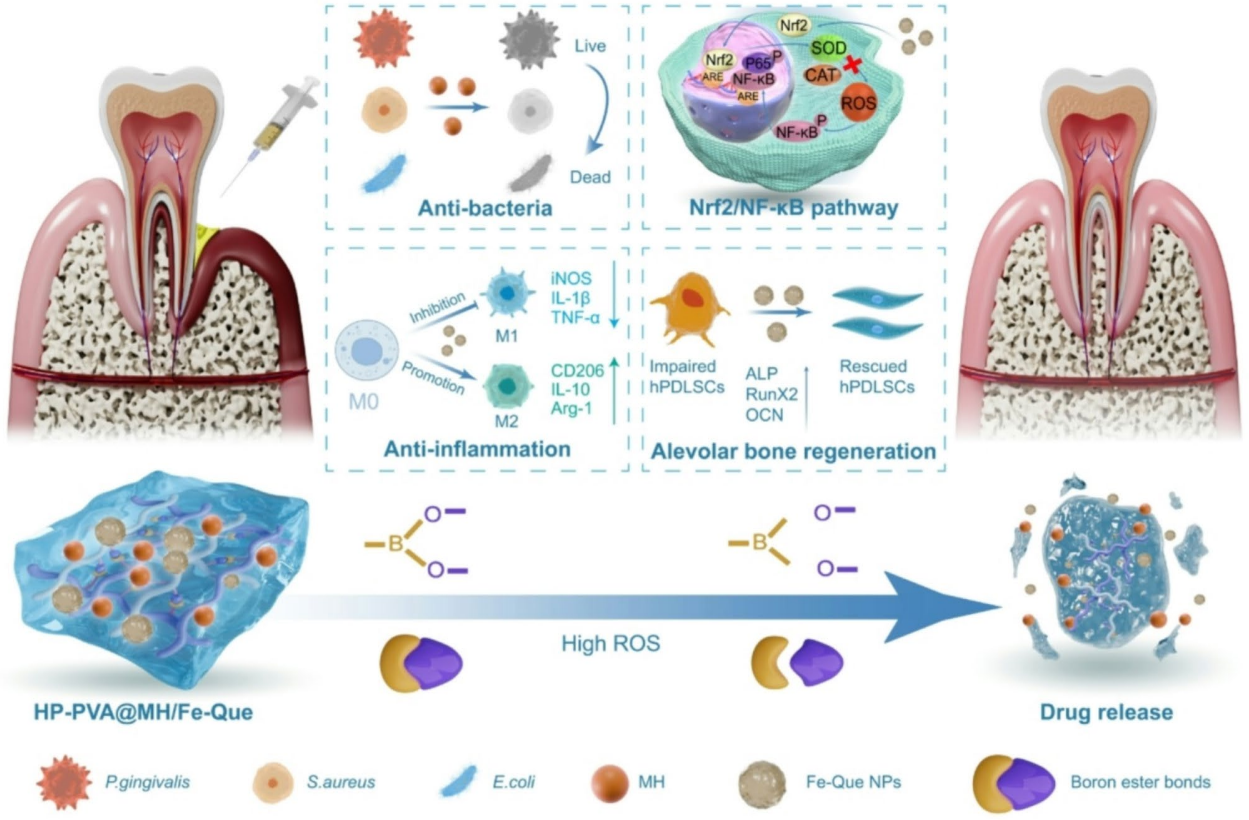

Keywords Periodontitis, ROS-responsive hydrogels, Drug delivery, Antibacterial, Anti-inflammation

Introduction

Periodontitis, one of the most common dental diseases, is a chronic inflammatory disease caused by bacteria that leads to gum detachment, periodontal pocket formation, and alveolar bone resorption [1]. If periodontitis is not treated promptly and effectively, it will gradually destroy the supporting tissues of the teeth and eventually lead to tooth loss [2]. Currently, the primary therapy for periodontitis involves the mechanical removal of bacteria and dental calculus through scaling and root planing (SRP) [3]. However, due to the complex anatomical structure of teeth, mechanical debridement cannot wholly remove subgingival pathogenic bacteria and their metabolites [4]. Additionally, local infections and inflammation are challenging to eliminate, leading to limited regenerative capacity of periodontal bone tissue and difficulty reconstructing periodontal tissue structure [5]. Therefore, developing a strategy for rapid antibacterial action, effective inflammation relief, and promoting bone and tissue regeneration is central to periodontitis therapy.

Periodontal pathogens can produce a variety of enzymes, toxins, and toxic metabolites, which subsequently damage tissues and trigger inflammatory reactions, leading to periodontal tissue destruction, such as bone loss and attachment loss [6, 7]. Therefore, rapid elimination of periodontal pathogenic bacteria is a prerequisite for treating periodontitis. Various drugs are available to remove periodontal pathogenic bacteria, such as antibiotics, antimicrobial peptides, and metal-based nanoparticles [8–11]. In clinical practice, minocycline hydrochloride (MH) is a commonly used topical agent for periodontal pockets. MH not only has high antibacterial activity against periodontal pathogens but also has collagenase-inhibiting properties. Many studies have shown that low doses of MH can significantly reduce inflammation at the periodontal site, thereby improving the success of periodontitis treatment [12, 13]. Therefore, MH is an ideal drug for the antibiotic treatment of periodontitis. However, the use of MH alone has many limitations, such as rapid drug loss, which cannot achieve a slow release and rapid antibacterial effect. Therefore, loading the MH into a carrier such as nanoparticles, microspheres, or hydrogels is necessary.

Hydrogel is a soft and flexible three-dimensional network, similar to the porous structure of extracellular matrix (ECM), thus facilitating regenerative tissue repair [14]. Injectable hydrogels made from biocompatible and biodegradable matrices can be injected into irregularly shaped periodontal pockets for sustained and stable drug release after encapsulating bioactive molecules and drugs [15]. In recent years, "smart hydrogels" have been developed to enable targeted and effective therapies by introducing stimulus-sensitive groups that respond to disease-specific microenvironments (e.g., hypoxia, low pH, and high levels of ROS) [16]. Therefore, for the high ROS microenvironment of periodontitis, the ROS-responsive hydrogel can achieve accurate on-demand drug release at the site of periodontitis lesions, reducing the frequency of dosing and side effects [17]. Phenylboronic acids, a member of the Lewis acid group, can form reversible and dynamic boronic ester bonds with compounds containing 1,3-diol groups [18, 19]. Boron ester bonds are susceptible to ROS, and in the high ROS environment of periodontitis, hydrogels based on boron ester bonds degrade, leading to accelerated drug release [17]. Therefore, we would like to load the antimicrobial drug MH into a hydrogel based on borate bonding to achieve responsive release of MH in the high ROS environment of periodontitis.

The balance between bacteria and host is disrupted at the site of periodontitis lesions. Excess ROS are produced, which activates multiple pro-inflammatory signaling pathways, leading to an increase in the ratio of M1 to M2 macrophages and the production of a large number of pro-inflammatory cytokines, such as interleukin-6 (IL-6), tumor necrosis factor-alpha (TNF-α), and interleukin-1β (IL-1β) [20–22]. M1 macrophages secrete pro-inflammatory cytokines to promote bone resorption and have the potential to differentiate into mature osteoclasts [23–26]. Conversely, M2 macrophages promote the differentiation of mesenchymal stem cells (MSCs) into mature osteoblasts and enhance bone mineralization [27, 28]. In addition, a high ROS environment induces cellular senescence, which in turn leads to MSC death, ultimately affecting the regenerative potential of the tissue [29, 30]. Therefore, regulating ROS levels in the periodontal microenvironment, protecting hPDLSCs from oxidative stress damage, rescuing their osteogenic capacity, and promoting M2 macrophage polarization is essential for treating periodontitis. Quercetin (Que) is a polyphenolic flavonoid compound found in onions, grapes, berries, cherries, broccoli, and citrus fruits [31]. Attributed to its inherent reducing structure, such as catechol groups, Que has outstanding anti-inflammatory and antioxidant activities, which can effectively eliminate ROS and inhibit the polarization of macrophages to the M1 phenotype while promoting their polarization to the M2 phenotype, thus reducing oxidative damage and facilitating tissue regeneration [32–34]. However, Que has poor water solubility, low bioavailability, and poor stability, which limits its use in the treatment of periodontitis [35]. It was found that Que coordination with metal ions to synthesize nanoparticles (NPs) improves their solubility and stability [36, 37]. Additionally, Nrf2 (Nuclear factor erythroid 2-related factor 2) and NF-κB (Nuclear factor kappa B) play a crucial role in regulating oxidative stress and inflammatory responses, which are essential for maintaining cellular redox balance and responding to inflammation [38–40]. Therefore, we hope to incorporate Que-metal nanoparticles as anti-inflammatory agents into ROS-sensitive hydrogels to explore their potential for treating periodontitis *via* the Nrf2/NF-κB signaling pathway.

In this study, as shown in Scheme 1, the ultra-small Fe-Que NPs were first formed by the coordination of quercetin with low-toxicity iron ions. In addition, hyaluronic acid (HA) was grafted with 3-aminophenyl borate (HA-PBA, HP), which was further reacted with the 1,3-diol group of poly (vinyl alcohol) (PVA) to form a borate bond, resulting in the construction of hydrogels with ROS-responsive properties. MH and Fe-Que were introduced to prepare the HP-PVA hydrogel system (HP-PVA@MH/Fe-Que). In the high ROS environment of periodontitis, the borate bond was broken, accelerating the release of MH and Fe-Que. The small molecule MH rapidly kills bacteria, and then the Fe-Que NPs scavenge ROS, reduce the inflammatory response of periodontal tissue, and alleviate alveolar bone resorption. The physical properties, drug release characteristics, antibacterial activity, and biocompatibility of the HP-PVA@MH/Fe-Que compound were evaluated in detail. This study demonstrated that the HP-PVA@MH/Fe-Que hydrogel initially rapidly inhibited bacterial growth through MH. Subsequently, Fe-Que scavenged ROS *via* the Nrf2/NF-κB pathway, regulated macrophage polarization to reduce pro-inflammatory factors and up-regulate anti-inflammatory factors, while also protecting hPDLSCs from ROS-induced damage and promoting osteogenic differentiation under oxidative stress. The ability of HP-PVA@MH/Fe-Que hydrogel to scavenge ROS and alleviate inflammation and alveolar bone resorption was also confirmed in a chronic periodontitis SD model. Therefore, with remarkable in vitro and in vivo therapeutic efficacy, HP-PVA@MH/Fe-Que hydrogel may have great potential for treating periodontitis.

Materials and methods

Materials

Ferric (III) trichloride hexahydrate ($FeCl_3 \cdot 6H_2O$), Polyvinylpyrrolidone (PVP, molecular weight: 10000 Da), and 3-amino phenylboronic acid (PBA) were purchased

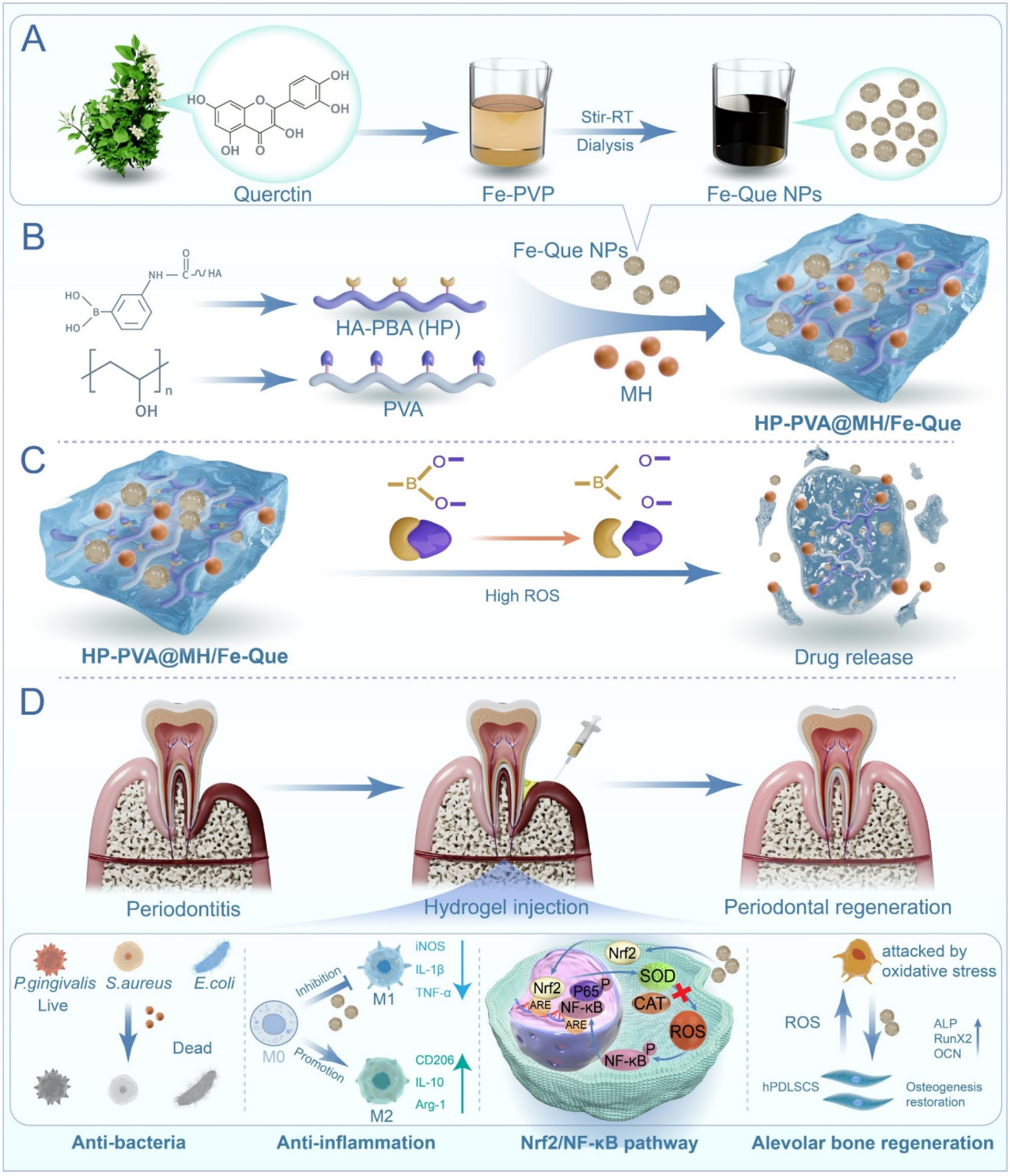

Scheme 1 Schematic diagram of the HP-PVA@MH/Fe-Que hydrogel synthesis and treatment of periodontitis. (**A**) Synthetic process of Fe-Que NPs. (**B**) Preparation of HP-PVA@MH/Fe-Que hydrogel. (**C**) ROS-triggered on-demand release of therapeutic agents in HP-PVA@MH/Fe-Que hydrogel. (**D**) HP-PVA@MH/Fe-Que hydrogel has multifunctional properties, including antibacterial, regulating Nrf2/NF-κB pathway to inhibit inflammatory and bone absorption relief for treating periodontitis

from Aladdin (Shanghai, China). Quercetin (Que) was obtained from Must Bio-Technology Co., Ltd (Chengdu, China). Hyaluronic acid (HA, molecular weight: 100000–200000 Da) and Polyvinyl alcohol (PVA, molecular weight: 31000–50000 Da) were purchased from Macklin (Shanghai, China). 1-(3-dimethylaminopropyl)-3-ethyl carbodiimide hydrochloride (EDC) and N-hydroxysuccinimide (NHS) were obtained from Heowns (Tianjin, China). Minocycline hydrochloride (MH) was purchased from MeilunBio (Liaoning, China). α-modified Eagle's Medium (α-MEM), high-glucose Dulbecco's Modified Eagle Medium (High glucose DMEM), RPMI 1640 Medium, 0.25% Trypsin-EDTA, and 10% Fetal Bovine Serum (FBS) were purchased from Gibco (CA, USA). Live/Dead® Viability Kit and Live/Dead bacterial staining kits were obtained from Thermo Fisher Scientific (MA, USA). Cell Counting Kit-8, 1% penicillin-streptomycin, and 4% paraformaldehyde were purchased from Beyotime (Beijing, China). 2',7'-dichlorofluorescein diacetate (DCFH-DA), 2,2-diphenyl-1-(2,4,6-trinitrophenyl) hydrazide (DPPH), 2,2′-azino-bis (3-ethylbenzthiazoline-6-sulfonic acid) (ABTS) were obtained from Solarbio (Beijing, China).

Synthesis and characterization of Fe-Que NPs

Fe-Que NPs were the coordination of iron ions with quercetin. Firstly, 20 mg of $FeCl_3{\cdot}6H_2O$ was dissolved in 1 mL of methanol, and 66 mg of PVP was dissolved in 5 mL of methanol, respectively. The two solutions were mixed and stirred for 5 min. Then, 10 mg of Que was added to 1 mL of methanol and mixed for 5 min. Finally, the Que solution was added to the above-mixed solution and stirred at room temperature for 3 h. The solution was placed in dialysis strips and dialyzed overnight with ultrapure water to remove excess iron ions, resulting in Fe-Que NPs. They were lyophilized in a freeze-dryer (Sientz-12 N, Ningbo, China) and stored at 4 °C for subsequent use.

The morphology and size of Fe-Que NPs were examined using transmission electron microscopy (TEM, JEM-2100, Tokyo, Japan). Dynamic light scattering (DLS) measurements of particle size distributions (Malvern, Nano ZS, UK). The UV-visible spectrophotometer (TU-1810, Shanghai, China) was used to determine the UV-visible near-infrared (UV-vis-NIR) spectra of $FeCl_3{\cdot}6H_2O$, Que, and Fe-Que NPs, respectively. The Fourier transform infrared (FTIR) spectra of Que and Fe-Que NPs were obtained using an FTIR spectrometer (WQF-530, Beijing, China) to evaluate the surface functional groups. The chemical states were determined by X-ray photoelectron spectroscopy (XPS, Shimadzu Kratos AXIS Ultra DLD, Nagoya, Japan).

Synthesis and characterization of HA modified by PBA (HA-PBA, named HP)

Liquor A was obtained by mixing 5.8 mL of acetic acid in 1 L of ultrapure water, and liquor B was 8.2 g of sodium acetate dissolved in 1 L of ultrapure water separately. Take 29.6 mL of liquor A, 70.4 mL of liquor B, and 100.0 mL of ultrapure water, and mix them well to get the acetic acid buffer solution with pH = 5.0. HA (1 g) was dissolved in 100 mL of buffer solution (pH = 5.0) under constant stirring, followed by adding 0.891 g of NHS, 1.495 g of EDC, and 0.684 g of PBA. All reaction mixtures were stirred at room temperature for 4 h. After the reaction was completed, the product was dialyzed in ultrapure water for 48 h, with the water being replaced twice daily to remove salts and unreacted substances from the solution. Finally, the product was freeze-dried to obtain the white flocculent HP.

The UV-vis-NIR spectrum of HA, PBA, and HP was measured using the UV-visible spectrophotometer (TU-1810, Shanghai, China). The FTIR spectra of HA, PBA, and HP were measured using the FTIR spectrometer (WQF-530, Beijing, China). The chemical structures of HA and HP were analyzed by proton nuclear magnetic resonance (^{1}H NMR), carried out on a 400 MHz Bruker Avance III (MA, USA). Furthermore, the degree of substitution was determined by the ratio of the integral of aromatic protons from the conjugated phenylboronic acid group (between 7.5 ~ 8 ppm, $-C_6H_4$) to the integral of the HA methyl proton peak (at 2.0 ppm, $-CH_3$).

Preparation and characterization of the hydrogels

Hydrogels were formed through boron ester dynamic bonding. Briefly, HP (2.5 wt%) and PVA (2.5 wt%) were prepared in ultrapure water to form a homogeneous mixture, respectively. Then, it is mixed in a volume ratio of 3:1 at room temperature to form HP-PVA hydrogels. The MH was dispersed in the PVA solution to prepare the hydrogel named HP-PVA@MH. The Fe-Que NPs were homogeneously dispersed in the HP solution to prepare the hydrogel named HP-PVA@Fe-Que. Then, HP-PVA@MH/Fe-Que hydrogels were prepared by simultaneously loading Fe-Que NPs and MH solution. The final concentration of Fe-Que NPs in the hydrogels was 500 μg/mL, and the final concentration of MH was 1 mg/mL. The hydrogels were observed macroscopically using the "inverted bottle method" to testify to the hydrogel formation. The hydrogels were lyophilized in the freeze-dryer for subsequent experiments.

The samples were fixed on a metal base and sprayed with gold under vacuum. Then, the microstructures of the samples were visually observed by field-emission scanning electron microscopy (SEM, Sigma 300, ZEISS, Germany), and the samples' surface elements

composition and distribution were detected by energy dispersive spectrometer (EDS) images.

The injectability, shape-adaptive, adhesive, and self-healing properties of the hydrogels

To analyze the injectability and observe the morphology of the hydrogel, the HP-PVA@MH/Fe-Que hydrogel was injected with a 2-mL syringe needle, and "SWMU" was written on a piece of paper for macroscopic observation. To further validate the injectability of the hydrogel, the injection force was analyzed using a mechanical testing machine (Instron Model 5965). The rheological analyses of the hydrogel, including storage modulus (G'), loss modulus (G"), and viscosity under different conditions (frequency sweep, strain sweep, and shear rate), were conducted using a rheometer (Discovery HR-2, TA Instrument, USA). The sample was tested by placing it between parallel plates (20 mm diameter, 1 mm gap) at 37 °C. G' and G" changes were evaluated at a fixed frequency (10 rad/s) to assess the effects of different strains. Additionally, the frequency dependence of G' and G" was analyzed at a fixed strain (1%) across a range of angular frequencies (0.1–100 rad/s). The viscosity of the hydrogel was measured across a shear rate range from 0.1 to 100 s^{-1} to evaluate its shear-thinning behavior.

Next, the HP-PVA@MH/Fe-Que hydrogel was injected into the mold. The state of its adaptation to the mold was observed every 30 s, and the shape of the original hydrogel (0 min) and the hydrogel adapted to the environment (2 min) was recorded. The adhesive properties of the hydrogels were assessed by observing whether they adhered to the heart, liver, spleen, lungs, and kidneys of SD rats and human orthodontic teeth after being moistened in PBS for 1 min. Moreover, the adhesion of hydrogels to fresh porcine gingiva and human premolar enamel was quantitatively assessed [41]. The porcine gingiva (length: 70 mm, width: 10 mm) was isolated and washed with PBS. Two pieces of porcine gingiva were then bonded together with hydrogel over an area of 10 mm × 10 mm, and the gingivae were left at room temperature for 15 min. The bonded samples were subsequently fixed on a materials testing system (INSTRON, USA) with a rate of 1 mm/min for the lap shear test to evaluate the ultimate adhesive strength. In addition, human premolars were embedded in plaster in the same way as described above. The formula for calculating the adhesion stress is as follows:

$$\text{Adhesion strength} = \mathrm{F_{max}}/\mathrm{S}$$

Where F_{max} and S are the maximum value of the force on the stress curve and the adhesion area of the two porcine gingivae or human premolar teeth enamel, respectively. Then, the self-healing property was evaluated using the HP-PVA hydrogel, which was divided into two sections and dyed red and green with food dye solutions. The sections were then pressed together to ensure complete adhesion in the cross-section. After 1 min, the hydrogel was observed and photographed to determine if it fractured when stretched on both sides.

ROS-responsive properties of the HP-PVA@MH/Fe-Que hydrogels

2 mL of HP-PVA@MH/Fe-Que hydrogel was loaded into a sample bottle. Then, 1 mL of different concentrations of hydrogen peroxide (H_2O_2, 0, 100, and 1000 μM) was added. The changes in the hydrogel were photographed and recorded after 3 h. The liquid in the bottle was discarded, and the hydrogels were freeze-dried under vacuum conditions. The hydrogel microstructural changes were observed by SEM (Sigma 300, ZEISS, Germany).

Degradation behavior of HP-PVA@MH/Fe-Que hydrogels in vitro

1 mL of freshly prepared HP-PVA@MH/Fe-Que hydrogel was injected into a glass vial containing PBS solutions with different H_2O_2 concentrations (0, 100, and 1000 μM). At various time intervals, the samples were photographed.

In vitro drug release in response to ROS levels from the HP-PVA@MH/Fe-Que hydrogels

The release of MH from HP-PVA@MH/Fe-Que hydrogel under different concentrations of H_2O_2 solutions was determined in vitro. 2 mL of the HP-PVA@MH/Fe-Que hydrogel was put into the sample bottle, with 5 mL of H_2O_2 solutions (0,100,1000 μM), and the release medium was collected at different time points. The absorbance at 364 nm was measured by a UV-visible spectrophotometer (TU-1810, Shanghai, China) to evaluate the release rate of MH.

In vitro antibacterial activity assays of the hydrogels

Hydrogels were evaluated for their antibacterial activity against *Staphylococcus aureus* (*S. aureus*), *Escherichia coli* (*E. coli*), and *Porphyromonas gingivalis* (*P. gingivalis*). The HP-PVA, HP-PVA@Fe-Que, HP-PVA@MH, and HP-PVA@MH/Fe-Que hydrogels were placed on 24-well plates. Next, 1 mL bacterial suspension (1×10^6 CFU/mL) was added to the surface of the hydrogels and co-cultured at 37 °C for 2 h. The PBS treatment was the control group. Then, the bacterial suspensions (100 μL) were collected, and *S. aureus* and *E. coli* were coated on LB solid medium, with *P. gingivalis* coated on a blood plate, cultured at 37 °C for 24 h to form visual colony units. Photos of LB or blood plates were taken, and the number of colonies was counted.

Moreover, the suspensions were stained using bacterial live/dead staining kits (Thermo Fisher Scientific, MA, USA). The working solution was prepared by adding SYTO 9 (1.5 μL) and propyl iodide (PI, 1.5 μL) to 1 mL of PBS. The bacterial precipitate was obtained by centrifuging the above bacterial suspension at 12,000 rpm for 10 min. Subsequently, it was incubated with the working solution at room temperature in the dark for 15 min before being observed under the fluorescence microscope (DMI8, Leica, Germany).

To further evaluate the antibacterial activity of the hydrogels, a zone of inhibition (ZOI) assay was conducted. In addition to *S. aureus, E. coli, P. gingivalis*, and the key pathogen *Streptococcus mutans* (*S. mutans*), which is associated with oral biofilm formation, was tested to assess the effectiveness of the hydrogels against oral-specific bacteria. The sterilized hydrogels were immersed in PBS at 37 °C for 24 h to obtain hydrogel extracts [8]. A 100 μL aliquot of bacterial stock in the logarithmic growth phase (*S. aureus, E. coli, P. gingivalis*, and *S. mutans*) was evenly spread onto agar plates. Sterile filter paper discs (6 mm diameter) were prepared using a round leather punch and soaked in the respective hydrogel extracts. Control discs soaked in 1× PBS and those soaked in hydrogel extracts were placed onto the inoculated agar plates using sterile tweezers. The plates were incubated at 37 °C for 24 h under aerobic conditions (*S. aureus, E. coli*, and *S. mutans*) or anaerobic conditions (*P. gingivalis*). After incubation, the diameter of the inhibition zones was measured using a ruler, and images of the agar plates were captured. All experiments were performed in triplicate, and the antibacterial activity was determined based on the average diameter (mm) of the inhibition zones formed around the paper discs.

The biocompatibility test of the hydrogels

Cell culture

HPDLSCs, human gingival fibroblasts (HGFs), RAW264.7, L929, and human immortalized epidermal cells (HaCaTs) were used as model cells to assess the cytotoxicity of hydrogels. L929 cells were cultured in RPMI 1640, while RAW264.7, HGFs, and HaCaTs were cultured in high-glucose DMEM medium, with 10% FBS and 1% penicillin-streptomycin. All cultures were incubated at 37 °C in a humidified atmosphere of 5% CO_2 and 95% relative humidity. The cell medium was replaced every 3 days and treated with 0.25% Trypsin-EDTA when the cells reached 70–80% confluency.

The hPDLSCs were derived from healthy premolars of orthodontic patients aged 12–18. All the young permanent teeth used in this study were taken from The Affiliated Stomatological Hospital of Southwest Medical University, with informed consent of patients and guardians, and approved by the Ethics Committee (20220819002). The dental tissue was soaked and repeatedly rinsed with PBS containing different concentrations of penicillin-streptomycin. Then, the middle-third of the periodontal tissue in the root was scraped with a sterile blade, centrifuged, transferred to an inverted culture bottle, cultured in a cell incubator containing 5% CO_2 at 37 °C, and turned over after 4 h. The complete medium required for cell culture was α-MEM containing 10% FBS and 1% penicillin-streptomycin. After the cells climbed out of the tissue, the medium was changed every 3 days and passaged when the cell reached 60–70% confluency. Flow cytometry (FACSCalibur, CA, USA) was utilized to evaluate the differentiation potential of hPDLSCs using antibodies against CD34, CD45, CD90, and CD105 (BioLegend, CA, USA). All the subsequent experiments used the 3rd to 5th generation cells in the logarithmic growth phase.

The cytocompatibility of the hydrogels

The cell viability was evaluated by CCK-8 assay and live/dead staining of hPDLSCs, HGFs, RAW264.7, L929, and HaCaTs to assess the cytotoxicity of the hydrogel. Firstly, the hydrogels (HP-PVA, HP-PVA@MH, HP-PVA@Fe-Que, HP-PVA@MH/Fe-Que) were irradiated under ultraviolet light overnight, soaked in alcohol for 0.5 h, and washed three times with PBS. Next, 50 mg/mL of hydrogel was immersed in different complete media (RPMI 1640, high-glucose DMEM, α-MEM) for 24 h, and the leachates were filtered through sterile filters to obtain the extracts.

HPDLSCs, HGFs, RAW264.7, L929, and HaCaTs, were seeded at a density of 3×10^3 cells/well on 96-well plates. After 1 day, the complete medium was replaced with the hydrogel leachates, and the incubation was continued for the 1st, 3rd, and 5th days, respectively, for assay using the CCK-8 assay kit (Beyotime, China). After washing with PBS, the CCK-8 working solution was added to the medium, and the cells were co-cultured at 37 °C for 1.5 h in the dark. Then, the absorbance value (OD value) at 450 nm was detected using a microplate reader (TECAN Infinite M200PRO, China).

In addition, the cells were seeded at a density of 5×10^3 cells/well on 24-well plates. After 1 day, the complete medium was replaced with the hydrogel extracts and co-cultured for the 1st, 3rd, and 5th days. Then, the cells were incubated for 0.5 h with the configured cell live/dead stain in the dark and observed under a fluorescence microscope (Leica, DMi8, Germany). Moreover, hPDLSCs were co-cultured with the hydrogel for 24 h (the Control group was not co-cultured with the hydrogel). Subsequently, compatibility and morphology were determined using live/dead cell staining, CCK-8 assay, and FITC staining.

The hemocompatibility test of the hydrogels

The blood compatibility of hydrogel was evaluated with rabbit red blood cells. First, rabbit blood was put into a centrifuge tube containing sodium citrate solution, centrifuged at 1000 rpm for 10 min to obtain red blood cells, then washed with PBS 3 times and diluted to a final concentration of 5% (v/v). Hydrogels and red blood cell suspension were combined in a 1.5 mL centrifuge tube and incubated at 37 °C for 1 h. Following this, the mixture was centrifuged at 1000 rpm for 10 min. Next, the supernatant was transferred to a 96-well plate with 100 μL per well. The absorbance value (OD value) at 545 nm was detected by a microplate reader (TECAN Infinite M200PRO, China), and the optical images were taken under a fluorescence microscope (Leica, DMi8, Germany). The positive control group was 0.1% Triton X-100, while the negative control group consisted of PBS.

Free radical scavenging ability and antioxidant capacity of the hydrogels

DPPH and ABTS radical scavenging assay

The radical scavenging performance of the hydrogels was analyzed using DPPH and ABTS kits. The DPPH and ABTS working solutions were prepared, mixed with the hydrogel extract, and incubated for 0.5 h in the dark. Vitamin C (VC) served as the positive control group, while the extract provided with the kit was the blank group.

Then, the DPPH free radical scavenging rates of different hydrogels were assessed using the UV-visible spectrophotometer (TU-1810, Shanghai, China) to record the OD values at 515 nm and the UV-vis-NIR spectra in the range of 480–560 nm. Next, the OD values at 405 nm of each sample were recorded, and the UV-vis-NIR spectra in the range of 400–800 nm were determined to evaluate the ABTS free radical scavenging rates.

$$\begin{aligned}&\text{Scavenging ability of positive control}\,(\%)\\&=\left[\left(A_{\text{blank}}-A_{\text{VC}}\right)/A_{\text{blank}}\right]\times 100\%\end{aligned}$$

$$\begin{aligned}&\text{Scavenging ability of sample}\,(\%)\\&=\left[\left[A_{\text{blank}}-\left(A_{\text{sample}}-A_{\text{control}}\right)\right]/A_{\text{blank}}\right]\times 100\%\end{aligned}$$

Where A_{blank} is the absorbance of 1 mL of working solution plus 50 μL of water, A_{VC} is the absorbance of 1 mL of working solution added to 50 μL of a VC solution (1 mg/mL), A_{sample} is the absorbance of 1 mL of working solution added to 50 μL of the supernatant of the sample, and $A_{control}$ is the absorbance of 1 mL of ethanol added to 50 μL of the supernatant of the sample.

Cytoprotective effects against oxidative stress

DCFH-DA evaluated the ability of different groups of hydrogels to eliminate intracellular ROS, and the effect of rescuing cells from oxidative stress and restoring their vitality was assessed by cell live/dead staining and the CCK-8 assay. In short, L929 and RAW264.7 cells were plated at a density of 2×10^4 cells/well in 24-well plates and incubated for 1 day. Then, the culture medium was swapped with the hydrogel extracts. After continuing the culture for 24 h, 100 μM H_2O_2 was added for 2 h. DCFH-DA working solution (1:1000) or cell live/dead dye solution was added, incubated for 0.5 h in the dark, and observed under a fluorescence microscope. ImageJ quantified the fluorescence intensity of DCFH-DA staining. Then, ROS fluorescence in FITC channels was measured by flow cytometry (ACEA NovoCyteTM 2070R, USA). Furthermore, RAW264.7 cells were plated in 96-well plates, subjected to the previously described treatment, and replaced with the prepared CCK-8 working solution. After incubation for 1.5 h, the OD value at 450 nm was detected by a microplate reader (TECAN Infinite M200PRO, China).

Moreover, the capacity of various hydrogels to eliminate ROS was assessed by measuring fluorescence intensity using a Multimodal Small Animal Live Imaging System (ABL X6, Tanon). RAW264.7 cells were seeded at a density of 2×10^4 cells/well on 12-well plates and treated the cells as we did before. Then, fluorescence imaging was also performed using the Multimodal Small Animal Live Imaging System (excitation filter, 440–510 nm; emission filter, 490–570 nm).

Macrophage polarization assessment of the hydrogels

Immunofluorescence (IF) staining and flow cytometry were used to detect the immunoregulatory effects of different hydrogels on RAW264.7 cell phenotypes. RAW264.7 cells were seeded on 24-well plates at a density of 4×10^4 cells/well. After incubation for 12 h, the complete induction was replaced with 100 ng/mL LPS (Sigma-Aldrich, USA) or 20 ng/mL IL-4 (Peprotech, USA) for 24 h, followed by treatment with hydrogel extracts for 24 h. Next, they were fixed in 4% paraformaldehyde for 20 min and treated with 0.5% Triton X-100 for 10 min. They were blocked with 5% goat serum for 1.5 h and then incubated overnight at 4°C with anti-iNOS (1:100, Proteintech, China) or anti-CD206 (1:100, Proteintech, China) primary antibodies. After rewarming for 0.5 h on the second day, FITC-labelled goat anti-rabbit IgG (1:200, Cell Signaling Technology, USA) was incubated for 60 min in the dark. Then, DAPI was stained for 10 min, and the anti-fluorescence quencher was sealed and stored in the dark at 4°C. Immunofluorescence images were obtained by laser scanning confocal microscope (CLSM600, Sunny Optical Technology, China), and 3D heatmaps were evaluated using ImageJ.

Moreover, RAW264.7 cells were planted in a six-well plate and treated according to the aforementioned

method. Then, the cells were digested with 0.25% Trypsin-EDTA and centrifuged at 1000 rpm for 5 min, with pre-cooled PBS 3 times. Subsequently, the cells were kept in the dark for 15 min with anti-CD86 (105005, Biolgend) and CD206 (147105, Biolgend). Finally, the samples were detected by flow cytometry (ACEA NovoCyteTM 2070R, USA), and FlowJo analyzed the data.

In vitro antioxidant and anti-inflammatory mechanism of the hydrogels through the regulation of the Nrf2/NF-κB pathway

The expression of nuclear factor erythroid-2 related factor 2 (Nrf2) and nuclear factor kappa-B (NF-κB) were examined by IF staining. RAW264.7 cells were seeded on 24-well plates at a density of 4×10^4 cells/well. After incubation for 12 h, the complete induction was replaced with 100 ng/mL LPS (Sigma-Aldrich, USA) for 24 h, followed by treatment with hydrogel extracts for 24 h. Next, RAW264.7 cells were performed using anti-Nrf2 (1:100, Cell Signaling Technology, USA) and NF-κB (1:100, Cell Signaling Technology, USA). Other IF staining procedures were the same as above. Images were captured, and 3D heatmaps were evaluated using ImageJ.

Then, the expression levels of inflammatory factors and antioxidant enzyme genes in RAW264.7 cells were detected by Quantitative Real-Time PCR (qRT-PCR). In brief, RAW264.7 cells were seeded at a density of 5×10^4 cells/well in 6-well plates and treated as described in this section. Total RNA was isolated using a SteadyPure quick RNA extraction kit (AG21023, Agbio, China) and converted into cDNA by the Evo M-MLV RT Kit (AG11728, Agbio, China). Then, qRT-PCR was conducted on a CFX96 Touch Real-Time PCR Detection System (Bio-Rad Laboratories, California, USA) using SYBR Green *Pro Tap* HS Premix (AG11701, Agbio, China). Using *β-actin* as the internal reference gene, the relative expression levels of each target gene were calculated using the $2^{-\Delta\Delta Ct}$ method. The primer sequences for the *IL-1β, TNF-α, IL-10, Arg-1, SOD-1*, and *CAT* genes are presented in Table S1.

Further, western blot (WB) analysis was performed to evaluate the related expression levels of antioxidant protein (Nrf2), NF-κB signaling pathway proteins (NF-κB and p-NF-κB), and β-actin. Macrophage cells were processed in the same manner as for qRT-PCR. Then, total proteins were extracted with Radio Immunoprecipitation Assay (RIPA) buffer (EpiZyme, China) containing proteinase and phosphatase inhibitors (1:100, Beyotime, China) on ice. Lysates extracted with RIPA buffer were sonicated and then centrifuged at 12,000 rpm. Subsequently, the protein concentrations were quantified by using the BCA protein assay kit (EpiZyme, China). An equal amount of boiled protein digest was loaded onto the Sodium dodecyl sulfate-polyacrylamide gel electrophoresis (SDS-PAGE) for protein separation, followed by transfer to a polyvinylidene fluoride (PVDF) membrane. Following a 15-min block at room temperature using Protein Free Rapid Blocking Buffer (EpiZyme, China), the membranes were subsequently exposed to primary antibodies against Nrf2 (1:1000, Cell Signaling Technology), NF-κB (1:1000, Cell Signaling Technology) p-NF-κB (1:1000, Cell Signaling Technology) and β-actin (1:5000, Proteintech, China) at 4 °C overnight. Next, the membranes were incubated with secondary antibodies after washing three times, followed by visualization of the immunoreactive protein bands using OI600 MF Touch (BIO-OI, China).

In vitro osteogenic differentiation assessment of the hydrogels

The hPDLSCs were planted on the 12-well plate coated with 1% gelatin in advance. Then, the culture medium was swapped with the hydrogel extracts. After continuing the culture for 24 h, 300 μM H_2O_2 was added for 2 h. Next, the culture medium was substituted with the prepared osteogenic induction solution. After 5 days of culture, they were fixed with 4% paraformaldehyde for 20 min, added with the configured BCIP/NBT alkaline phosphatase working solution, stained for 0.5 h in the dark, and then observed with a type microscope (SZN71, Sunny Optical Technology, China). After culture for 21 days, the calcium nodules were stained with ARS solution.

In addition, the hPDLSCs were seeded on 24-well plates and treated the cells as we did before. Samples collected for 7 days were stained for Runx2, whereas those cultured for 21 days were stained for the late osteogenic protein osteocalcin (OCN). For IF, hPDLSCs were performed using anti-RUNX2 (1:100, Cell Signaling Technology, USA) and anti-OCN (1:100, Proteintech, China). Moreover, the cytoskeleton morphology after H_2O_2 treatment was observed by fluorescence microscope. They were fixed with 4% paraformaldehyde for 20 min and treated with 0.5% Triton X-100 for 10 min. Then, they were incubated with FTIC (1:100, Cytoskeleton) for 1 h, stained with DAPI, and sealed with an anti-fluorescence quencher. In addition, the hPDLSCs and hydrogels were co-cultured in the presence of hydrogen peroxide to observe the morphological changes of the cells. The control group consisted of hPDLSCs cultured in a complete medium without H_2O_2 treatment. In the H_2O_2 group, 300 μM H_2O_2 was added to the culture medium to induce oxidative stress. HP/PVA, HP/PVA@MH, HP/PVA@Fe-Que, and HP/PVA@MH/Fe-Que hydrogels were co-cultured with hPDLSCs, with 300 μM H_2O_2 added simultaneously. After 24 h, cells were labeled with DAPI and FITC fluorescence staining, and their adhesion and morphology on the hydrogel surfaces were observed

using laser confocal microscopy. Finally, the fluorescence microscope was used to visualize the IF images, and 3D topographic maps were evaluated using ImageJ.

In vivo treatment in periodontitis model

In vivo establishment of periodontitis model in rats

All animal experiments were approved by the Ethics Committee of Southwest Medical University and conducted according to the guidelines established by the Animal Care Committee (Document No. 20230705-005). Following 1 week of acclimatized feeding, thirty male Sprague-Dawley rats, aged 6 weeks and weighing between 180 and 220 g, were randomly allocated into six groups: (1) Control group: no treatment, (2) Periodontitis group: treated with ligation and an injection of *P. gingivalis*, (3) HP-PVA group: periodontitis treated with HP-PVA hydrogels, (4) HP-PVA@MH group: periodontitis treated with HP-PVA@MH hydrogels, (5) HP-PVA@Fe-Que group: periodontitis treated with HP-PVA@Fe-Que hydrogels, (6) HP-PVA@MH/Fe-Que group: periodontitis treated with HP-PVA@MH/Fe-Que hydrogels. Rats were anesthetized using isoflurane (2% in 100% oxygen), and a 0.2 mm archwire was securely placed beneath the gums of the bilateral maxillary first molars. *P. gingivalis* (1×10^9 CFU/mL, 20 μL) was injected into the palatal gingiva between the first and second molars every three days. After 2 weeks, the ligated archwire was removed, and hydrogels or saline (10 μL) were injected into the palatal gingival sulcus of the maxillary molar every three days.

In vivo antioxidant property

One week following the hydrogel treatment, the rats were anesthetized. DCFH-DA (1.8 mg/kg) was injected into the palatal gingiva between the first and second maxillary molars. After 30 min, images were obtained by a Multimodal Small Animal Live Imaging System (excitation filter, 440–510 nm; emission filter, 490–570 nm).

Micro-CT analysis

After 2 and 4 weeks, the animals were harvested for their maxilla, which was collected and fixed in 4% paraformaldehyde for one week. The samples were then scanned using a micro-CT system (nanoVoxel-100, Tianjin, China). The three-dimensional digitized models and two-dimensional digitized images were evaluated and reconstructed using the RediAnt DiCOM Viewer software. The distance between the cementoenamel junction and the alveolar bone crest (CEJ-ABC) was measured to estimate the extent of the buccal and sagittal alveolar bone loss.

Histology and immunohistochemistry

The collected maxillary samples were fixed in 4% paraformaldehyde, decalcified in 10% ethylene diamine tetraacetic acid (EDTA) for one month, dehydrated in gradient alcohol, and embedded in paraffin. Afterward, these paraffin samples were made into sections at 4 μm thickness. Hematoxylin and eosin staining (H&E) and Masson staining were performed according to instructions. The IL-1β and TNF-α expression in the periodontal tissue were evaluated using an immunohistochemistry method. Slides were scanned with a digital pathology slide scanner (KF-PRO-002, China), and observed using K-Viewer (1.7.0.23) X64. Moreover, IF staining, including iNOS, CD206, Nrf2, P65, Runx2, and OCN, was measured. Staining was visualized using CaseViewer. The observation areas were selected between the roots of the first and second molars.

Statistical analysis

All data were presented as mean ± standard deviation (SD) and the significance among multiple groups was examined by the one-way analysis of variance (ANOVA) using GraphPad Prism 9.0. Statistically significant values include $^{*}P < 0.05$, $^{**}P < 0.01$, $^{***}P < 0.001$, and $^{****}P < 0.0001$.

Results and discussion

Synthesis and characterization of Fe-Que NPs

In the synthesis of Fe-Que NPs, quercetin was dissolved in methanol and added to a PVP solution containing iron ions to improve the dispersion of Fe-Que NPs (Fig. 1A). The solution underwent a rapid color change from yellow to black upon adding quercetin, indicating successful coordination between the iron ions and the phenolic group of quercetin. The methanol solution containing Fe-Que NPs was dialyzed overnight to eliminate excess iron ions. Subsequently, Fe-Que NPs with high water solubility and stability were successfully obtained (Fig. 1B). TEM analysis revealed that Fe-Que NPs were spherical, ultra-small particles with uniform distribution and a size of less than 10 nm (Fig. 1C). Subsequent particle size analysis indicated a range of 1 to 3 nm for Fe-Que NPs (Fig. 1D). In addition, the mean particle size measurements by DLS were approximately 2.10 ± 0.66 nm, as illustrated in Fig. S1. The UV–vis spectra for iron ions, quercetin, and Fe-Que NPs were presented in Fig. 1E. Free Fe^{3+} exhibited clear absorption peaks at 248 nm and 368 nm, Quercetin showed absorbance at 256 nm and 370 nm, while the peak intensity of Fe-Que NPs notably decreased in the range of 200–600 nm [37]. The FTIR spectral analysis of Fe-Que NP showed that the intensity of the vibrational peaks at 1150 ~ 1200 cm^{-1} corresponding to the HO-C functional group decreased (Fig. 1F), which indicated that Fe^{3+} was successfully coordinated with the quercetin HO-C molecule [36]. In addition, the chemical composition and state of Fe-Que NPs were analyzed using XPS. The full XPS spectrum revealed that

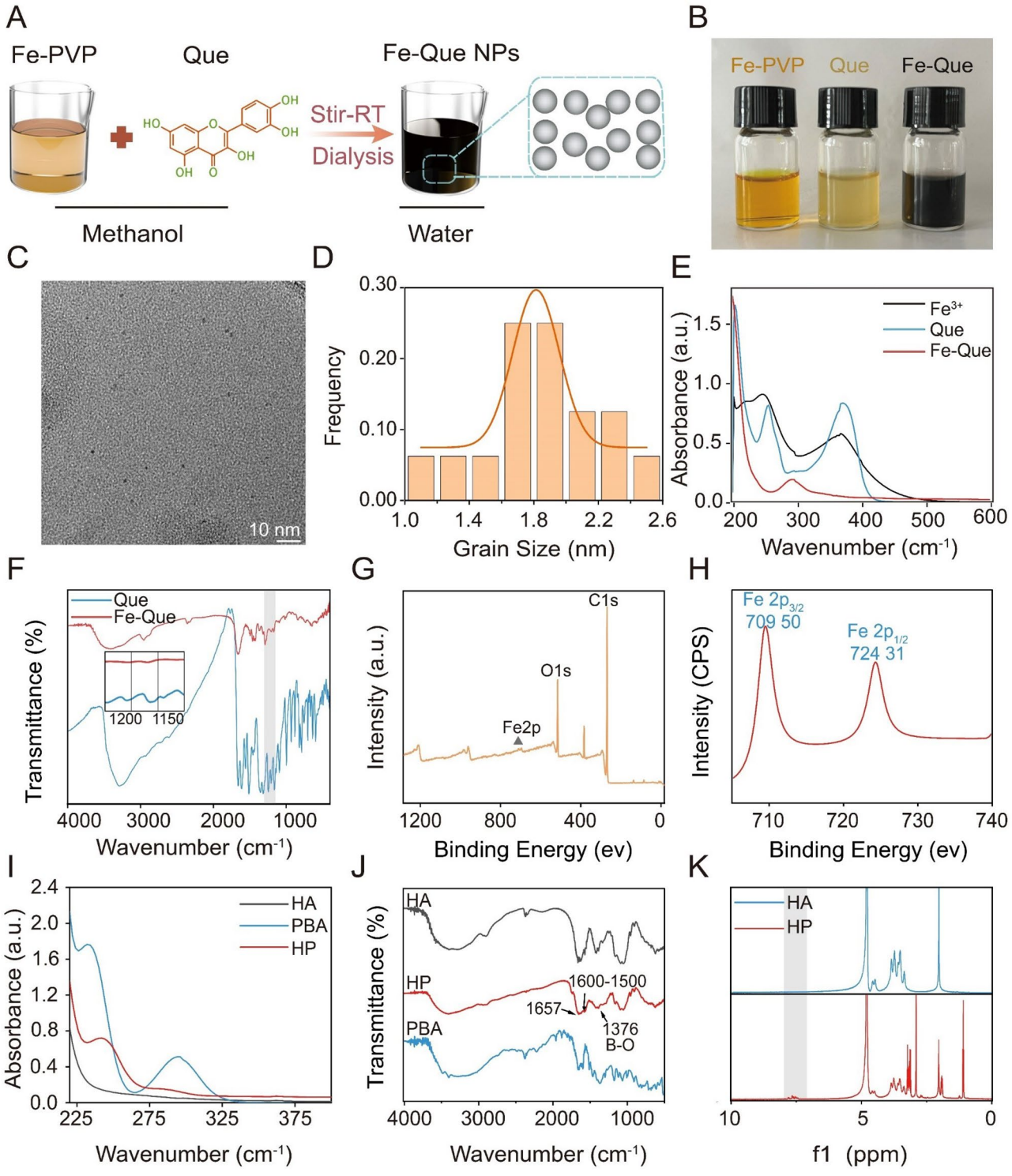

Fig. 1 Synthesis and characterization of Fe-Que NPs and HP. (**A**) Schematic diagram of the synthesis of Fe-Que NPs. (**B**) Picture of the synthetic materials, including Fe-PVP, Que, and Fe-Que NPs. (**C**) TEM and (**D**) Grain size of Fe-Que NPs. (**E**) UV-vis absorption spectra of $FeCl_3{\cdot}6H_2O$, Que, and Fe-Que NPs. (**F**) FTIR spectra of Que and Fe-Que NPs. (**G**) Full XPS spectrum of Fe-Que NPs. (**H**) High-resolution spectra of ferric ions in Fe-Que NPs. (**I**) UV-vis absorption spectra and (**J**) FTIR spectra of HA, PBA, and HP. (**K**) ^{1}H NMR spectra of HA and HP

Fe-Que NPs mainly comprise carbon, oxygen, and iron (Fig. 1G). Furthermore, Fig. 1H showed two prominent binding energy peaks at 709 eV and 724 eV corresponding to the $2p_{3/2}$ and $2p_{1/2}$ orbitals of iron ions, suggesting that the oxidation state of iron ions in the Fe-Que NPs remained unchanged. The results from the aforementioned studies collectively demonstrated the successful preparation of Fe-Que NPs.

Synthesis and characterization of HP

Firstly, HP was synthesized by grafting HA with 3-aminophenyl boronic acid. The UV-vis spectra of HA, PBA, and HP are shown in Fig. 1I. HA exhibited no UV-vis absorption peak in the range of 220–400 nm, while PBA displayed an absorption peak at 232 nm corresponding to the benzene ring, as well as a noticeable absorption peak at 260–325 nm attributed to the amino and benzene ring p-π conjugate system. HP showed a characteristic absorption peak of the benzene ring at 242 nm similar to that of PBA. However, the absorption peak at 260 ~ 325 nm almost disappeared due to the weakened p-π conjugation effect between the amino group and benzene ring after grafting onto HA. This result confirmed that PBA was successfully grafted onto the HA segment. In order to further characterize the changes in the HA structure after modification, it was analyzed by FTIR spectra (Fig. 1J). Comparing the infrared spectrum of HA, there is no obvious change in the characteristic absorption peak of HP, but the aromatic C = O and C = C stretching vibration can be observed at 1657 cm^{-1} and 1500 ~ 1600 cm^{-1}, respectively. The B-O stretching vibration at 1376 cm^{-1}, further verified the grafting of 3-aminophenyl boronic acid and the success of the amidation reaction [39]. The ^{1}H NMR spectra of HA and HP before and after the grafting reaction are presented in Fig. 1K. At chemical shifts of 1.9 ppm and 3.2–4.5 ppm, both HA and HP exhibited identical proton absorption peaks corresponding to the methyl and methylene groups on HA, respectively. The appearance of a new proton peak between 7.0 ppm and 8.0 ppm confirmed the successful grafting of PBA onto HA [42]. The degree of substitution was determined by calculating the ratio between the integral of aromatic protons from the conjugated phenylboronic acid group (between 7.0 and 8.0 ppm, $-CH_4$) to that of methyl protons from HA (1.9 ppm, $-CH_3$), resulting in a calculated grafting efficiency of phenylboronic acid groups onto HP at approximately 15%.

The Preparation and characterization of the HP-PVA@MH/Fe-Que hydrogels

Considering the high ROS level in the periodontitis microenvironment, in this study, a ROS-responsive smart hydrogel was designed to achieve dual delivery of antibiotics and anti-inflammatory ultra-small NPs, which can improve antibacterial performance, accelerate the removal of ROS and alleviate inflammation and bone resorption. As depicted in Fig. 2A, a hydrogel network was formed by establishing dynamic borate ester bonds (highly sensitive to ROS) between the diol group structures on PVA and the phenylboronic acid groups on HP. Figure 2B shows the state of HP-PVA@MH/Fe-Que hydrogel before and after gelation. Next, the microscopic morphology of the hydrogels was observed by SEM. As depicted in Fig. 2C, all the hydrogels exhibited interconnected pores and uniform three-dimensional porous structures, facilitating the encapsulation of biologically active molecules and protecting them from degradation. Moreover, it ensured efficient nutrient and oxygen transport, promoting cellular penetration, proliferation, and new tissue formation. Furthermore, EDS map analysis revealed a homogeneous distribution of elements C, N, O, B, and Fe throughout the HP-PVA@MH/Fe-Que hydrogel (Fig. 2D), providing evidence for the successful loading and dispersion of Fe-Que nanoparticles within the hydrogel.

Injectability, adaptability, adhesion, and self-healing properties are essential properties of hydrogels for local drug delivery in periodontal pockets [43]. The injectability feature facilitates the efficient penetration of hydrogels into narrow and deep periodontal pockets, providing spatiotemporal control of therapeutic drug release through material degradation and drug diffusion [8]. Figure 2E showed that the HP-PVA@MH/Fe-Que hydrogel could be easily transferred into a syringe and extruded from a needle (0.5 × 20 mm) to form an "SWMU" shape without any clogging. Fig. S2A showed the setup where the syringe was fixed in the lower tensile grip, and the syringe's piston was compressed using the upper compression platform. The injection rate was controlled by adjusting the transverse speed of the compression platform to achieve an injection speed of 2 mL/min. The plunger force was measured using a 50-N load cell. As shown in Fig. S2B, the maximum injection force for the HP-PVA@MH/Fe-Que hydrogel at an injection speed of 2 mL/min was 21.88 N. Fig. S3A showed that the storage modulus (G') of HP-PVA@MH/Fe-Que hydrogel were greater than the loss modulus (G") across the strain range of 0.1-100%. As shown in Fig. S3B, G' were all significantly higher than G" across a range of angular frequencies (0.1–100 rad/s), indicating good structural stability after gelation [44]. Moreover, within a shear rate range of 0.1–100 s^{-1}, the viscosity of HP-PVA@MH/Fe-Que hydrogel significantly decreased with increasing shear rate, demonstrating typical shear-thinning behavior (Fig. S3C). The HP-PVA@MH/Fe-Que hydrogel exhibits excellent injectability, favorable elasticity, shear-thinning behavior, and appropriate structural stability, meeting

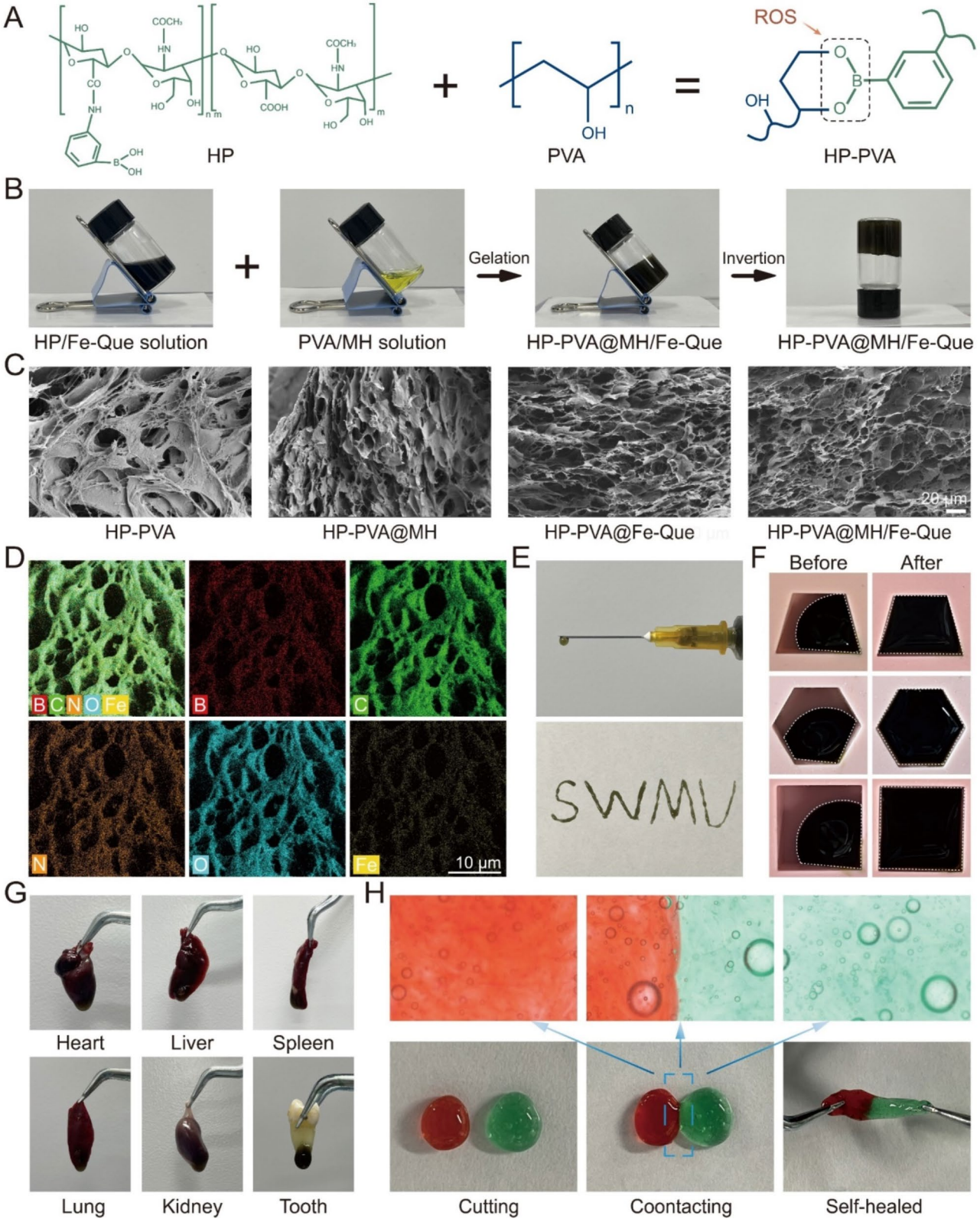

Fig. 2 Preparation and characterization of the HP-PVA@MH/Fe-Que hydrogels. (**A**) Schematic diagram of the synthesis of hydrogels. (**B**) Photographs of the HP-PVA@MH/Fe-Que hydrogel before (left) and after (right) gelation. (**C**) SEM images of the different hydrogels. (**D**) EDS mapping of the HP-PVA@MH/Fe-Que hydrogel. Photographs of the (**E**) injectability, (**F**) shape-adaptability, and (**G**) adhesion of the HP-PVA@MH/Fe-Que hydrogel. (**H**) Photographs of the self-healing properties of the HP-PVA hydrogel

the requirements for local stability and precise treatment during periodontal therapy.

In periodontitis, periodontal tissue is destroyed irregularly. Hydrogel possesses both gel-like elasticity and fluidity, exhibiting excellent shape adaptability, which enables the hydrogel to fit perfectly with the damaged periodontal tissue and adapt to irregularly shaped periodontal defects [45]. As shown in Fig. 2F, the HP-PVA@MH/Fe-Que hydrogel could be reshaped into different shapes, which could be used to fill different defects and had good adaptability. After being injected into the periodontal pocket, the hydrogel is subjected to constant washing by gingival fluid and saliva, so it should have certain adhesion properties to adhere to the periodontal tissue and prolong its retention time within the periodontal pocket [46]. The HP-PVA@MH/Fe-Que hydrogel exhibited a firm adhesion to the dental sulcus and internal organs, including the heart, liver, spleen, lungs, kidneys, and the root of the first premolar tooth (Fig. 2G). To further evaluate the tissue adhesion of the hydrogel, a standardized in vitro lap-shear test was conducted using porcine gingiva, and the hydrogel's adhesion to tooth enamel was assessed (Fig. S4A, S4B, S4D, and S4E). The results showed that MH and Fe-Que loading did not affect the adhesive properties of the hydrogel, and the adhesion strength of HP-PVA@MH/Fe-Que to pig gingiva was about 9.07 ± 1.65 kPa, and to enamel was about 8.40 ± 1.11 kPa (Fig. S4C and S4F). Furthermore, when the hydrogel is filled in the defective areas of the periodontal tissue, external forces may cause the hydrogel to break, but the rapid self-healing ability helps improve the hydrogel's adaptability to complex defect patterns [47]. Figure 2H visualized the self-healing performance of the HP-PVA hydrogel. The HP-PVA hydrogel was cut into 2 pieces and dyed red and green, respectively. After 1 min, the reassembled hydrogel was stretched, and it maintained its complete shape without breaking, indicating that the hydrogel had a good self-healing performance.

ROS-responsive behavior drug release kinetics, and in vitro degradation behavior of the hydrogels

The imbalance between ROS and the antioxidant defense system can lead to oxidative stress, a key signal molecule in the development of periodontitis [48]. During the development of periodontitis, the ROS levels were closely related to the degree of tissue damage in the periodontal tissue [49]. Therefore, designing a ROS-responsive hydrogel as a drug delivery system may be an effective strategy for the local treatment of periodontitis. By responding to ROS levels within the periodontal environment, the hydrogel can achieve precise on-demand drug release and effectively reduce ROS in the periodontal microenvironment to accelerate periodontal healing. Borate bonds can be oxidized by H_2O_2 at physiological pH and temperature [50]. Fig. S5A shows the reaction mechanism of hydrogel to ROS. Therefore, we treated the hydrogels with different H_2O_2 concentrations (0, 100, and 1000 μM) to investigate the degradation and drug release of the hydrogels to study their therapeutic effects on periodontitis. As shown in Fig. S5B, the samples were observed with different H_2O_2 concentrations (0, 100, and 1000 μM) for 3 h. The liquid in the sample bottle had different intensities of yellow, with the deeper the yellow indicating a higher concentration of H_2O_2. This result suggested that H_2O_2 increased the oxidation of the borate bond and led to the disintegration of the hydrogel. The SEM image of the frozen-dried sample (Fig. S5C) showed that as the concentration of H_2O_2 increases, the pore size of the hydrogel increases, and the three-dimensional network structure of the hydrogel gradually disintegrates in the oxidative environment. This result also indicated that the borate ester bonds in the hydrogel degraded in the oxidative environment, resulting in a decrease in the degree of cross-linking and an increase in the pore size of the hydrogel. Without H_2O_2 treatment, the drug is released due to the hydrolysis of borate bonds within the hydrogel over time. However, in the presence of H_2O_2, the hydrogel exhibits a responsive fracture due to oxidation of borate bonds, thereby accelerating drug release (Fig. S5D). In addition, the degradation behavior of HP-PVA@MH/Fe-Que hydrogels in PBS containing different concentrations of H_2O_2 (0, 100, and 1000 μM) was investigated. The results showed that the hydrogel morphology changed significantly with increasing H_2O_2 concentrations and reaction time, validating its responsiveness to ROS levels (Fig. S6). In summary, the HP-PVA@MH/Fe-Que hydrogel could achieve ROS-responsive degradation and accelerate drug release, which was beneficial for treating periodontitis.

In vitro antibacterial activity assays of the hydrogels

Bacteria are one of the factors that cause periodontitis, and their metabolic products can induce destructive resorption of periodontal tissues [51]. Even after standard periodontal treatment, certain bacterial hosts often persist on the root surface and need to be locally treated with antibiotics [52]. The MH has been widely used in clinical treatment. To study the effect of hydrogels on bacteria, the antibacterial performance of hydrogels was determined by the plate coating method, bacterial live/dead staining method and zone of inhibition (ZOI) assay. Figure 3A shows that the HP-PVA and HP-PVA@Fe-Que hydrogels did not have significant antimicrobial properties compared to the control group, as evidenced by the colony counts. However, only a few colonies could be seen in the HP-PVA@MH and HP-PVA@MH/Fe-Que groups for *S. aureus*, *E. coli*, and *P. gingivalis*. The results of bacterial colony counting were shown in Fig. 3B, C,

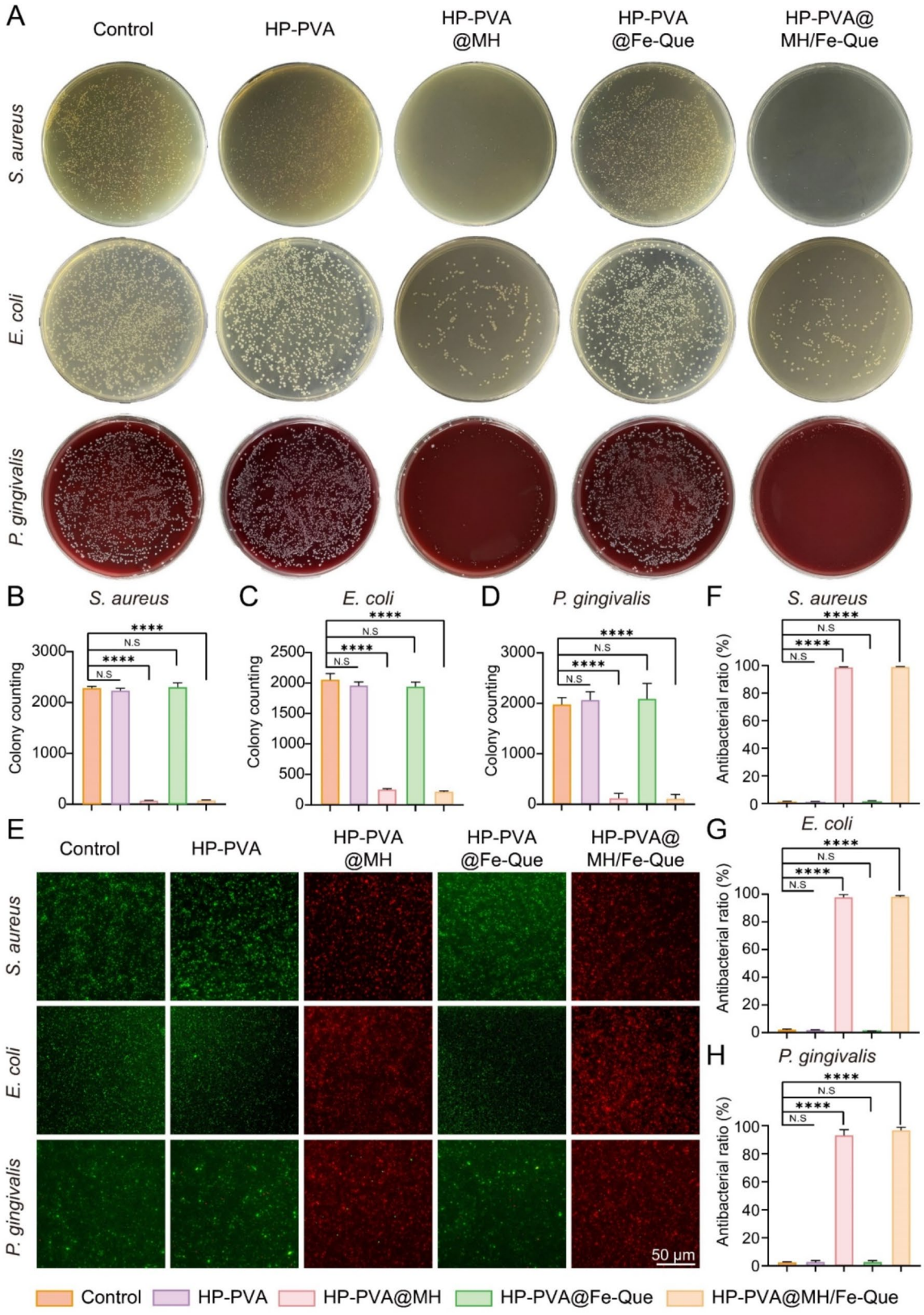

Fig. 3 In vitro antibacterial activity of the HP-PVA@MH/Fe-Que hydrogels. (**A**) Representative images of *S. aureus*, *E. coli*, and *P. gingivalis* colony-forming units. The pertinent statistical data for the quantification of bacterial colonies of (**B**) *S. aureus*, (**C**) *E. coli*, and (**D**) *P. gingivalis*. (**E**) The live/dead staining images of *S. aureus*, *E. coli* and *P. gingivalis*. Antibacterial rate of (**F**) *S. aureus*, (**G**) *E. coli* and (**H**) *P. gingivalis*

and D. The results demonstrated that the HP-PVA@MH and HP-PVA@MH/Fe-Que groups exhibited broad-spectrum antibacterial activity against both Gram-positive and Gram-negative bacteria, as well as the main pathogenic anaerobic bacteria responsible for periodontitis. Next, the bacterial live/dead fluorescence staining experiment was conducted to visually illustrate the hydrogels' antibacterial efficacy. As depicted in Fig. 3E, the control, HP-PVA, and HP-PVA@Fe-Que groups predominantly exhibited green fluorescence, indicating live bacteria presence; however, the HP-PVA@MH and HP-PVA@MH/Fe-Que groups displayed a significant amount of red fluorescence (indicating dead bacteria). Furthermore, these conclusions were supported by the live-dead fluorescence intensity analyses of *S. aureus*, *E. coli*, and *P. gingivalis* bacteria, respectively (Fig. 3F, G, H). To further evaluate the antibacterial activity of the hydrogels, a ZOI assay was conducted using *S. aureus*, *E. coli*, *P. gingivalis*, and the key oral pathogen *S. mutans*. The results indicated that the HP-PVA and HP-PVA@Fe-Que hydrogels did not form notable inhibition zones, while the HP-PVA@MH and HP-PVA@MH/Fe-Que groups exhibited clear inhibition zones against all tested bacteria, including *S. mutans* (Fig. S7). These findings were consistent with the bacterial colony counting results. Therefore, the hydrogel loaded with antimicrobial MH had outstanding antimicrobial capacity and acted on the initiators of periodontitis to achieve a great therapeutic effect.

The biocompatibility test of the hydrogels

Good biocompatibility is essential to prevent adverse effects of bio-scaffold materials on normal periodontal tissues and cells [53]. The extracts of the hydrogels were used to culture cells, and the effects on cell viability and proliferation were tested. The live/dead staining of cells at 1, 3, and 5 days (Fig. 4A and C, S8A, S8C, S8E) showed that most hPDLSCs, HGFs, RAW264.7, L929, and HaCaTs were alive, with only a few dead cells present.

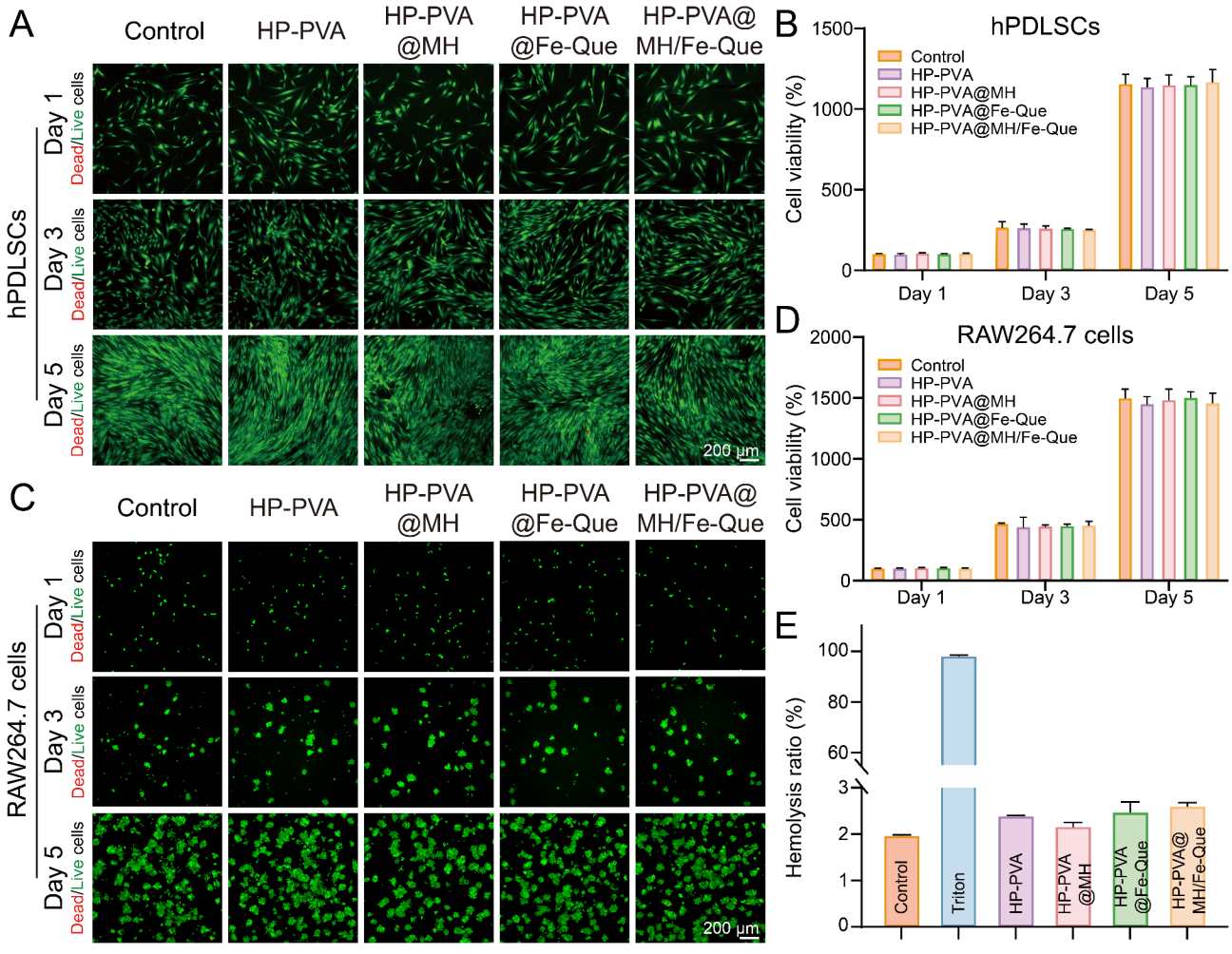

Fig. 4 Biocompatibility of the HP-PVA@MH/Fe-Que hydrogels. The Live/Dead staining images of (**A**) hPDLSCs and (**C**) RAW264.7 cells for 1, 3, and 5 days, respectively. The CCK-8 assays of (**B**) hPDLSCs and (**D**) RAW264.7 cells for 1, 3, and 5 days. (**E**) Hemolysis ratio of erythrocyte after incubating with the hydrogels

In addition, the number of cells increased gradually over time, with no difference from the control group, indicating that the hydrogels could not inhibit cell proliferation. Furthermore, the CCK-8 results on 1, 3, and 5 days showed no statistically significant difference in cell viability between the hydrogel treatment groups and the control group, which was consistent with the findings of the live/dead staining assay (Fig. 4B and D, S8B, S8D, S8F).

In addition, in order to show cell viability directly in the presence of the hydrogels for accurate biological interaction analysis, we co-cultured hPDLSCs on HP-PVA@MH/Fe-Que hydrogels. As shown in Fig. S9A and S9B, the hydrogel exhibited no apparent toxicity to hPDLSCs and demonstrated good biocompatibility. Furthermore, through DAPI and FITC fluorescence staining combined with laser confocal microscopy, it was observed that the cells were evenly distributed on the surface of the hydrogel and exhibited a well-spread spindle-shaped morphology, indicating excellent adhesion (Fig. S9C). Hence, the hydrogel had good cell compatibility.

Gingival bleeding is an important clinical symptom of periodontitis [9]. During the treatment of periodontitis, the hydrogel adheres to destroy the tissue surface in the periodontal pocket. From the perspective of biocompatibility, it must have a high level of blood compatibility. Compared with the control group, there was no obvious damage to the red blood cells in the hydrogel-treated group, while the red blood cells in the Triton X-100-treated group were ruptured (Fig. S10A, B). Figure 4E showed that the hemolysis rate of the hydrogel-treated group was less than 3% (< 5% is good blood compatibility), indicating that the hydrogel had good blood compatibility.

Free radical scavenging ability and antioxidant capacity of the hydrogels

Excessive ROS can exert cytotoxic effects and activate inflammatory factors, leading directly or indirectly to periodontal tissue destruction [54]. Therefore, scavenging excessive ROS is crucial for treating periodontitis and mitigating the damage to periodontal tissues [55]. Firstly, the DPPH free radical scavenging assay was used to evaluate the antioxidant performance of the hydrogels (Fig. 5A). The DPPH free radical has a single electron, and its alcohol solution is purple with strong absorption at 515 nm. In the presence of antioxidants, the DPPH free radical is neutralized, causing the solution to lighten in color and the absorbance at 515 nm to diminish [56]. To a certain degree, the change in absorbance reflects the extent of free radical scavenging. The control group showed the highest absorbance and appeared purple, whereas the positive group had the lowest absorbance and exhibited a slightly yellow color. The HP-PVA and HP-PVA@MH groups demonstrated negligible capacity for DPPH free radical scavenging. Conversely, both the HP-PVA@Fe-Que and HP-PVA@MH/Fe-Que groups exhibited significantly reduced absorbance levels, displaying a color intermediate between that of the control and positive groups (Fig. 5B). Figure 5C illustrates the DPPH free radical scavenging activity of different hydrogel groups. The results indicated that the HP-PVA@Fe-Que and HP-PVA@MH/Fe-Que groups had superior DPPH scavenging rates at 77.07% and 78.15%, respectively.

Secondly, ABTS undergoes oxidation, forming a stable green cationic radical with its peak absorption at 405 nm [57]. When the sample is introduced to the ABTS radical solution, the antioxidant compounds interact with the ABTS radicals, resulting in a color change in the reaction system and a reduction in absorbance at 405 nm (Fig. 5D). Besides, the change of its absorbance within a certain range is proportional to the degree of free radicals being scavenged. As Fig. 5E showed, the absorbance of the control group exhibited the highest value and appeared green, while the positive group displayed the lowest absorbance with transparent color. The HP-PVA and HP-PVA@MH groups demonstrated negligible capacity for ABTS free radical scavenging. Conversely, the HP-PVA@Fe-Que and HP-PVA@MH/Fe-Que groups displayed a color intermediate between the control and positive groups, exhibiting significantly reduced absorbance levels. The ABTS free radical scavenging rates were consistent as described above (Fig. 5F).

In addition, the ability of hydrogels to scavenge ROS was further demonstrated by intracellular DCFH-DA staining [58]. In the control group, RAW264.7 cells showed the lowest fluorescence intensity, while the fluorescence intensity of the H_2O_2, HP-PVA, and HP-PVA@MH groups was stronger, indicating the presence of large amounts of ROS. However, the HP-PVA@Fe-Que and HP-PVA@MH/Fe-Que groups showed reduced fluorescence intensity, indicating a strong ROS-scavenging ability (Fig. 5G, H). A similar result was also observed in L929 cells (Fig. S11). Importantly, the results of flow cytometry showed that the HP-PVA@Fe-Que and HP-PVA@MH/Fe-Que groups significantly reduced the ROS level in the RAW264.7 cells, which was highly consistent with the conclusions of microscopic observation, and further verified the excellent free radical scavenging ability (Fig. S12). We hypothesized that the HP-PVA@MH/Fe-Que hydrogels exhibit a high efficiency in scavenging ROS, which is attributed to the presence of phenolic and ketone groups in the quercetin structure.

Furthermore, the cytoprotective potential of hydrogel against oxidative stress-induced cell damage and their ability to restore cellular vitality was evaluated using live/dead cell staining and CCK-8 assay. As depicted in Fig. 5I, the substantial presence of red fluorescence

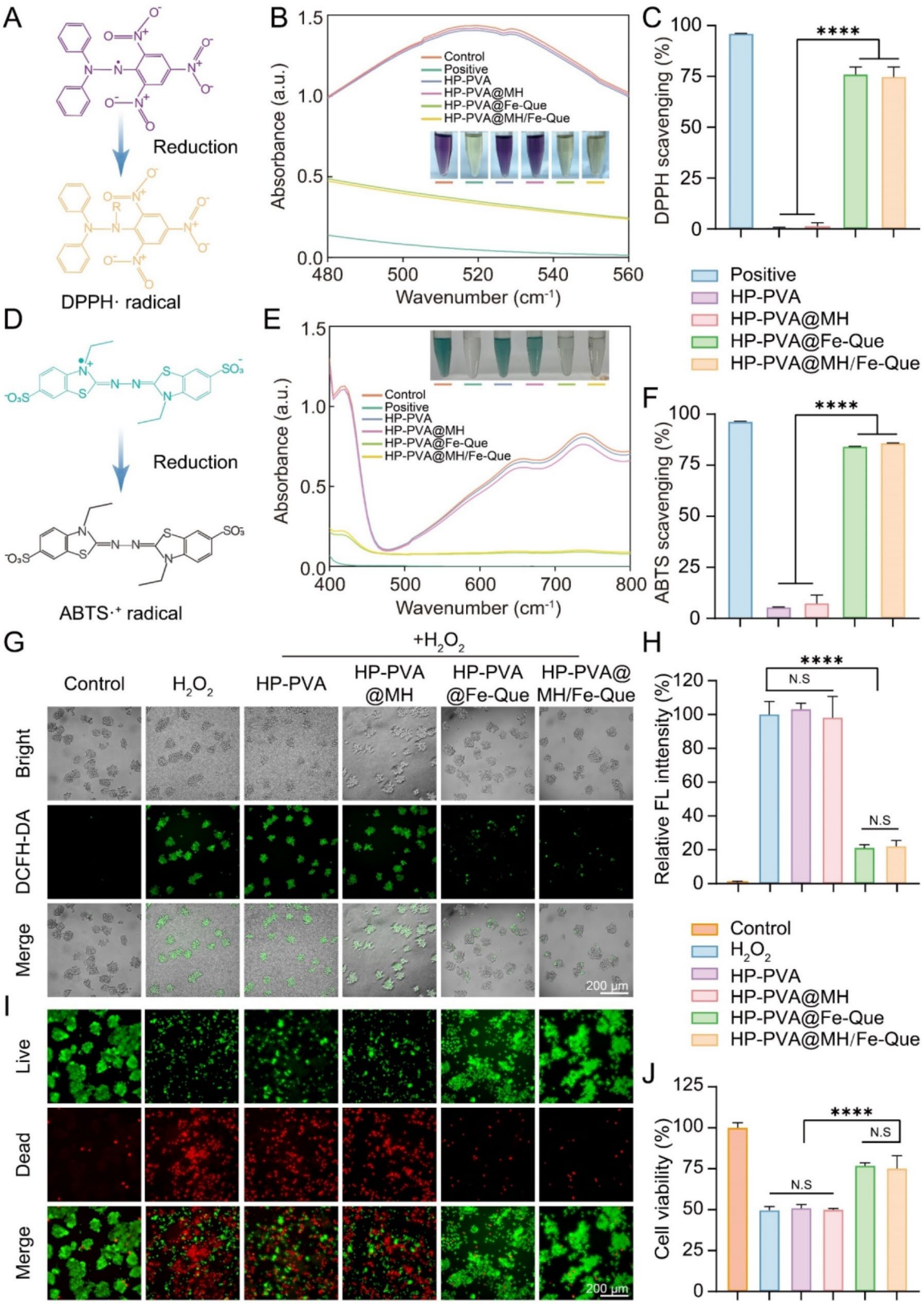

Fig. 5 Free radical scavenging ability and antioxidant capacity of the HP-PVA@MH/Fe-Que hydrogels under oxidative stress environment. (**A**) Schematic diagram showing the DPPH free radical scavenging assay. (**B**) Absorbance, photograph, and (**C**) DPPH scavenging ratio of the different hydrogels. (**D**) Schematic diagram showing the ABTS free radical scavenging assay. (**E**) Absorbance, photograph, and (**F**) ABTS scavenging ratio of the different hydrogels. (**G**) DCFH-DA staining, (**H**) fluorescent quantitative results, (**I**) Live/dead staining, and (**J**) CCK-8 assay of the RAW264.7 cell

(indicative of dead cells) was observed in the H_2O_2, HP-PVA, and HP-PVA@MH groups. However, the number of dead cells was significantly reduced in the HP-PVA@Fe-Que and HP-PVA@MH/Fe-Que groups. The results obtained from the CCK-8 analysis were consistent with the cell viability staining, revealing a significant decline in cell viability for the H_2O_2, HP-PVA, and HP-PVA@MH groups, while recovery was evident for the HP-PVA@Fe-Que and HP-PVA@MH/Fe-Que groups (Fig. 5J). These findings showed that HP-PVA@Fe-Que and HP-PVA@MH/Fe-Que hydrogels possessed remarkable cytoprotective properties capable of mitigating ROS-mediated deterioration in cellular vitality.

Macrophage phenotype regulation effect of the hydrogels

Excessive ROS activates multiple anti-inflammatory pathways in periodontitis, resulting in an increased ratio of M1 macrophages to M2 macrophages [59]. Inhibiting the transformation of macrophage phenotype to M1 macrophage phenotype (pro-inflammatory) and promoting the polarization to M2 macrophage phenotype (anti-inflammatory) is beneficial for alleviating inflammation and promoting osteoblast differentiation, which represents an essential therapeutic approach for the treatment of periodontitis. Therefore, to evaluate the effect of different hydrogels on macrophage polarization, we used LPS to promote polarization toward the M1 macrophage phenotype and IL-4 to drive polarization toward the M2 macrophage phenotype (Fig. 6A). The control group without induction exhibited regular circular morphology. In contrast, LPS-stimulated macrophages displayed short and filamentous pseudopodia morphology, and IL-4-stimulated macrophages demonstrated elongated morphology (Fig. 6B).

IF staining experiments were initially performed on macrophages to label M1 macrophages expressing inducible nitric oxide synthase (iNOS) and M2 macrophages expressing mannose receptor (CD206). As shown in Fig. 6C, the expression of iNOS in RAW264.7 cells significantly increased after LPS treatment. Compared to the LPS group, no significant difference in iNOS expression was observed in HP-PVA and HP-PVA@MH hydrogels. However, a significant reduction in iNOS expression was observed in the HP-PVA@Fe-Que and HP-PVA@MH/Fe-Que groups. As shown in Fig. 6E, the expression of CD206 in RAW264.7 cells increased after IL-4 treatment. Similarly, there was no significant variation observed in CD206 expression between the HP-PVA and HP-PVA@MH hydrogels compared with the IL-4 group; however, a substantial increase was observed in CD206 expression within the HP-PVA@Fe-Que and HP-PVA@MH/Fe-Que groups. Subsequently, additional flow cytometry analysis was performed to assess macrophage polarization (Fig. 6D, F). The findings demonstrated that the HP-PVA@Fe-Que and HP-PVA@MH/Fe-Que hydrogels effectively inhibited macrophage polarization towards M1 while promoting macrophage polarization towards M2, thereby facilitating inflammation resolution and tissue repair in periodontitis.

In vitro antioxidant and anti-inflammatory mechanism of the hydrogels by regulating the Nrf2/NF-κB pathway

Oxidative stress pathways play a crucial role in developing and progressing various diseases. Nrf2 is considered a key regulator of oxidative stress, which upregulates the expression of various antioxidant enzymes (such as SOD-1 and CAT) by binding to the antioxidant response element to scavenge excessive ROS, thus protecting cells from oxidative damage [60]. Nrf2 is also associated with macrophage polarization and the NF-κB pathway. Activation of the NF-κB pathway is crucial in chronic inflammation, promoting macrophage polarization towards the M1 type and increasing the expression of pro-inflammatory cytokines (such as IL-1β and TNF-α) [61]. The "Macrophage phenotype regulation effect of the hydrogels" results suggested that HP-PVA@MH/Fe-Que hydrogel could mediate macrophage polarization. Therefore, it can be inferred that HP-PVA@MH/Fe-Que hydrogel may regulate the Nrf2/NF-κB pathway to suppress oxidative stress, inhibiting macrophage polarization towards the M1 type and promoting polarization towards the M2 type. To investigate the potential role of the antioxidant and anti-inflammatory mechanisms of HP-PVA@MH/Fe-Que hydrogel, we conducted IF staining, qRT-PCR, and western blot to validate this hypothesis.

As shown in Fig. 7A, after LPS-induced inflammation, macrophages exhibited weaker Nrf2 fluorescence intensity, and the HP-PVA and HP-PVA@MH groups also showed similar fluorescence intensity; however, the Nrf2 fluorescence signal was significantly higher in the HP-PVA@Fe-Que and HP-PVA@MH/Fe-Que groups than in the LPS group. Conversely, for NF-κB, the fluorescence signal in the HP-PVA@Fe-Que and HP-PVA@MH/Fe-Que groups was lower than in the LPS group (Fig. 7B). According to the results shown in Fig. 7C-H, compared with the LPS group, the HP-PVA@Fe-Que and HP-PVA@MH/Fe-Que groups exhibited a downward trend in pro-inflammatory cytokine expression of *IL-1β* and *TNF-α*, and an upward trend in anti-inflammatory cytokine expression of *IL-10* and *Arg-1*. Additionally, the expression of antioxidant enzymes *SOD-1* and *CAT* was also enhanced in HP-PVA@Fe-Que and HP-PVA@MH/Fe-Que groups. These results suggested that the HP-PVA@Fe-Que and HP-PVA@MH/Fe-Que hydrogels possessed high antioxidant and anti-inflammatory capabilities.

Furthermore, western blot results showed that after the addition of LPS, the expression of Nrf2 decreased,

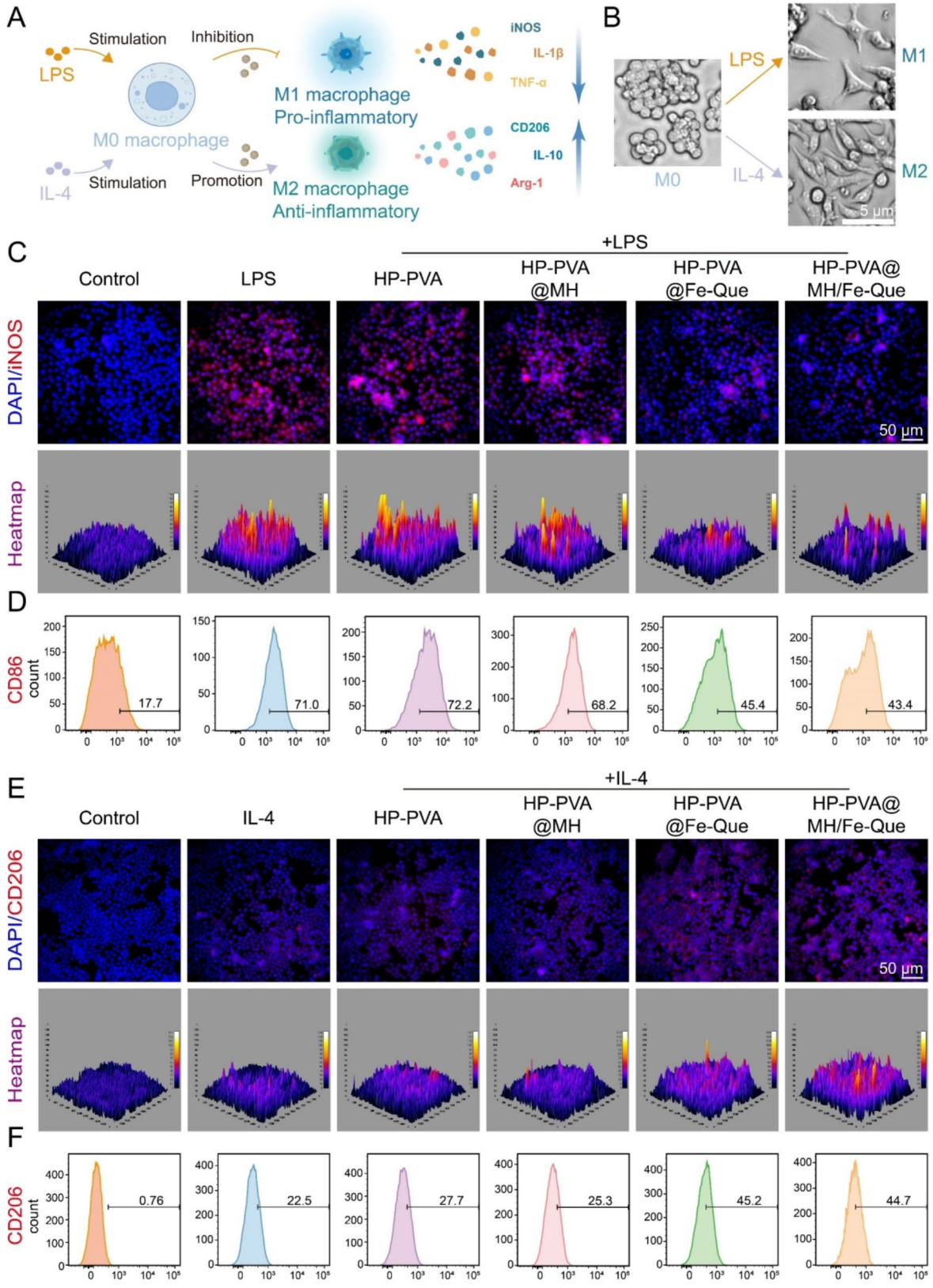

Fig. 6 HP-PVA@MH/Fe-Que hydrogels inhibit the polarization of macrophages toward the M1 phenotype while facilitating their polarization toward the M2 phenotype. (**A**) Schematic diagram showing the effect of the HP-PVA@MH/Fe-Que hydrogels on macrophage polarization. (**B**) Microscopic view of macrophages. IF images of (**C**) M1 (iNOS) and (**E**) M2 (CD206) macrophages maker. Flow cytometry analysis of (**D**) M1 (CD86) and (**F**) M2 (CD206) macrophage markers

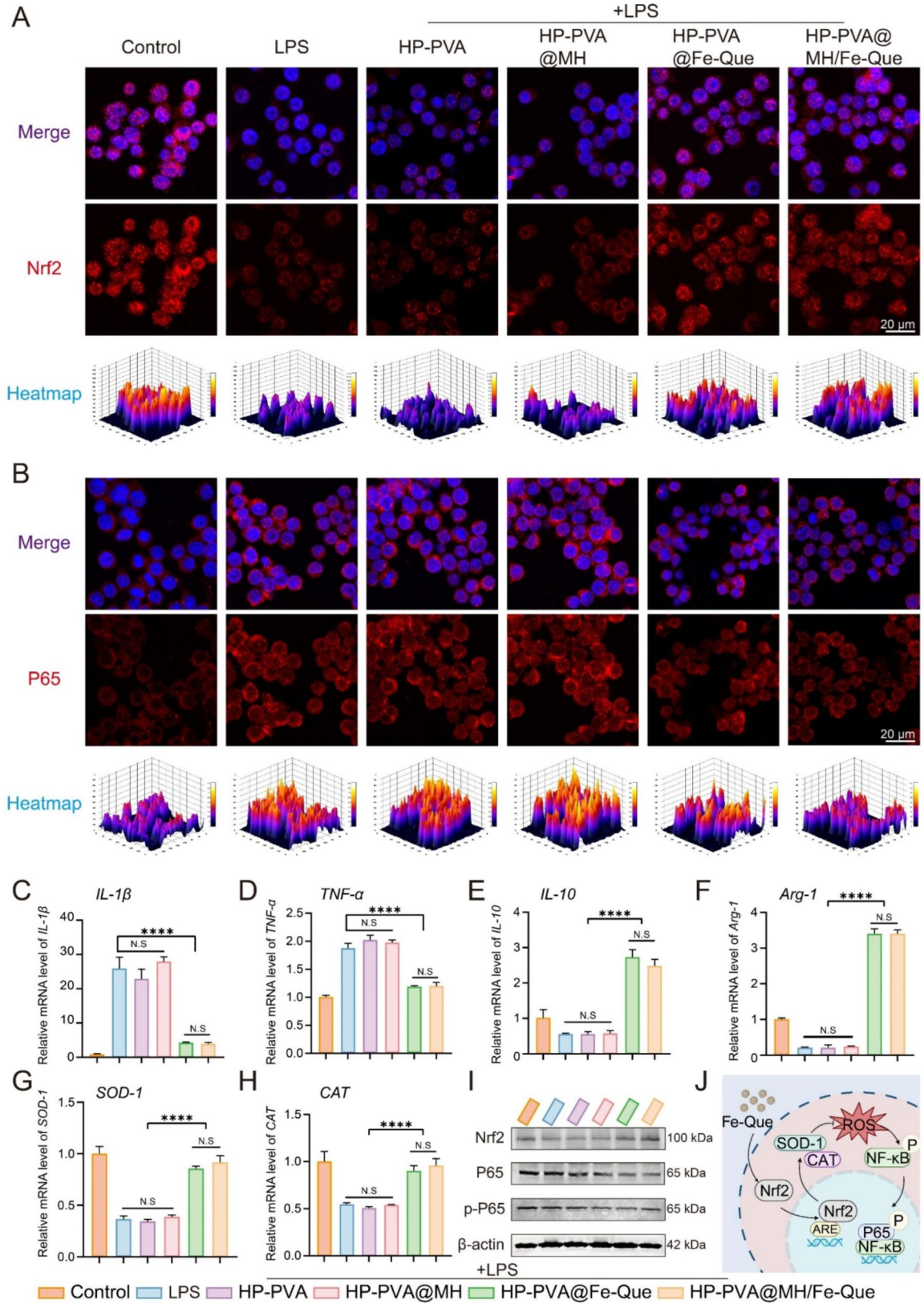

Fig. 7 HP-PVA@MH/Fe-Que hydrogels regulate the Nrf2/NF-κB pathway to exert antioxidant and anti-inflammatory effects in vitro. IF images of RAW264.7 cells for (**A**) Nrf2 and (**B**) NF-κB. QRT-PCR analysis of the relative mRNA level of (**C**, **D**) pro-inflammatory genes *IL-1β*, *TNF-α*; (**E**, **F**) anti-inflammatory genes *IL-10*, *Arg-1*; (**G**, **H**) antioxidant enzyme genes *SOD-1*, *CAT*. (**I**) Western blot detection of Nrf2, P65, and p-P65, with β-actin as the internal control. (**J**) The antioxidant and anti-inflammatory mechanism of HP-PVA@MH/Fe-Que hydrogel was presented as a schematic diagram

while the expression of Nrf2 in the HP-PVA@Fe-Que and HP-PVA@MH/Fe-Que groups increased. Conversely, the expression of P65 in the HP-PVA@Fe-Que and HP-PVA@MH/Fe-Que groups was weaker than that of the LPS group, as well as p-P65 (Fig. 7I). This result indicated that HP-PVA@MH/Fe-Que could enhance the expression of Nrf2 while reducing the levels of P65 and p-P65. Overall, the HP-PVA@MH/Fe-Que hydrogel can regulate the Nrf2/NF-κB pathway and influence the polarization of macrophages, thereby alleviating oxidative stress (Fig. 7J).

In vitro osteogenic differentiation assessment of the hydrogels

HPDLSCs have the potential for multidirectional differentiation, which is beneficial for alveolar bone regeneration [20]. As shown in Fig. S13, hPDLSCs displayed an elongated fusiform or spindle-shaped morphology and were morphologically comparable to the fibroblastic cells. Flow cytometric analysis revealed high expression levels of CD90 (99.97%) and CD105 (99.5%), while low expression levels of CD34 (0.08%) and CD45 (0.25%). These results indicated that the isolated hPDLSCs were well-differentiated mesenchymal stem cells derived from the periodontal tissue, with significant implications for periodontal tissue regeneration and repair. However, elevated ROS in the periodontal microenvironment induces oxidative stress, significantly inhibiting the osteogenic differentiation of hPDLSCs and destroying periodontal tissue [62]. Therefore, it is imperative to mitigate excessive ROS levels and preserve the osteogenic differentiation capacity of hPDLSCs to successfully repair periodontal tissue.

As illustrated in Fig. 8A, the HP-PVA@MH/Fe-Que hydrogel demonstrated its ability to protect hPDLSCs from osteogenic differentiation. The cellular morphology of each hydrogel group was evaluated under an H_2O_2-induced oxidative stress microenvironment (Fig. 8B). The control group displayed fibroblast-like cells with elongated spindle or fusiform shape, centrally located nuclei, and round or oval cytoplasmic structure. Conversely, the cells in the H_2O_2, HP-PVA, and HP-PVA@MH manifested a contracted and shrunken morphology under oxidative stress conditions. On the contrary, the cells in the HP-PVA@Fe-Que and HP-PVA@MH/Fe-Que regained their elongated spindle or fusiform shape, effectively mitigating the adverse effects of oxidative stress on hPDLSCs morphology. In addition, the hPDLSCs and hydrogels were co-cultured in the presence of hydrogen peroxide to observe the morphological changes of the cells (Fig. S14). The control group exhibited well-spindle-shaped cells. In the H_2O_2 group, cell morphology was significantly abnormal. Notably, the HP-PVA@Fe-Que and HP-PVA@MH/Fe-Que hydrogels, incorporating Fe-Que anti-inflammatory nanoparticles, exhibited superior cell compatibility by further enhancing cell adhesion and spreading through efficient ROS scavenging. Subsequently, osteogenic induction was performed within an oxidative microenvironment to investigate the impact of oxidative stress on the osteogenic behavior of hPDLSCs under hydrogel treatments. Alkaline phosphatase (ALP), an early marker for osteogenesis, serves as a reflection of osteoblast differentiation level [63]. Higher ALP activity indicates more pronounced differentiation from pre-osteoblasts into mature osteoblasts. Mineralized nodules serve as a key indicator of the differentiation and maturation of osteoblasts; therefore, Alizarin Red S (ARS) is used to stain or locate calcium deposits in tissues by forming an orange-red complex with calcium salts present in calcium carbonate or hydroxyapatite [64]. The ALP activity was significantly reduced in the H_2O_2, HP-PVA, and HP-PVA@MH compared to the control group, as shown in Fig. 8C. However, in the HP-PVA@Fe-Que and HP-PVA@MH/Fe-Que, there was a partial recovery of ALP activity between the control and H_2O_2 groups. Similar results were observed in the ARS analysis.

In addition, to further investigate the ability of HP-PVA@MH/Fe-Que hydrogel in rescuing hPDLSCs' osteogenic differentiation, immunofluorescence staining was conducted to evaluate the expression levels of Runx2 and OCN. Runx2 plays a crucial role in osteoblast differentiation and skeletal morphogenesis, exhibiting early high expression and nuclear localization [65]. OCN is an osteoblast's secreted protein that reflects its activity and bone formation capacity, serving as a late-stage marker for osteogenesis [66]. Compared to the control group, both Runx2 and OCN expressions were significantly reduced in the H_2O_2, HP-PVA, and HP-PVA@MH; however, they were partially restored in the HP-PVA@Fe-Que and HP-PVA@MH/Fe-Que groups (Fig. 8D). The results suggested that the osteogenic differentiation capacity of hPDLSCs was significantly impaired under the conditions of oxidative stress, whereas the HP-PVA@Fe-Que and HP-PVA@MH/Fe-Que hydrogels exhibited a partial rescue effect on the osteogenic differentiation potential, thereby enhancing bone regeneration for achieving periodontal tissue regeneration goals.

ROS removal ability of the hydrogels in vivo

Given the strong antibacterial, antioxidant, and anti-inflammatory effects of HP-PVA@MH/Fe-Que hydrogel on RAW264.7 cells and its favorable effect on osteogenic differentiation of hPDLSCs under oxidative conditions, we established models of experimental periodontitis in rats by using a combination of ligated archwires and injections of *P. gingivalis* to evaluate the therapeutic effects of HP-PVA@MH/Fe-Que hydrogel (Fig. S15). The experimental flowchart for in vivo studies is presented

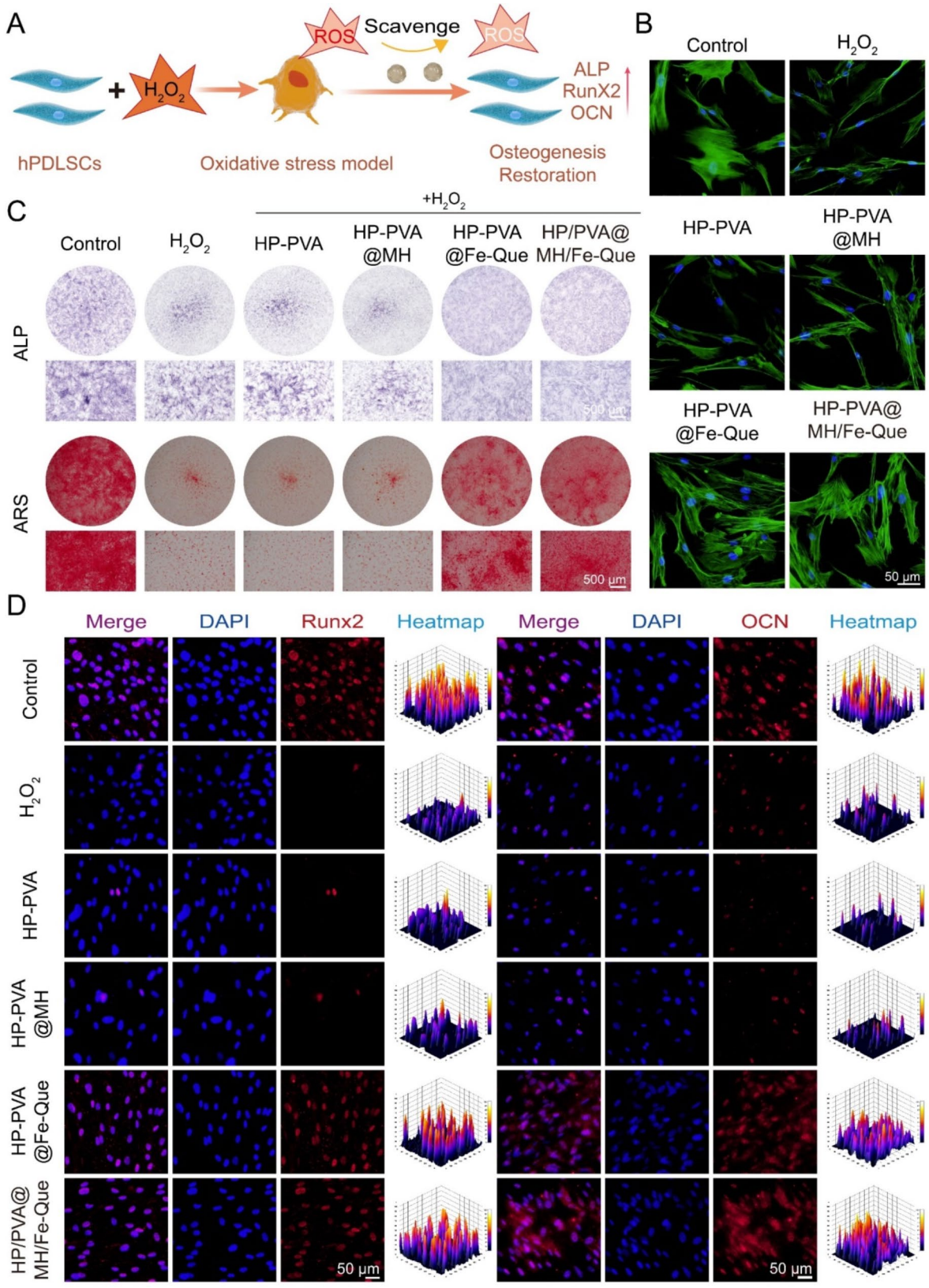

Fig. 8 HP-PVA@MH/Fe-Que hydrogels protected hPDLSCs from ROS attack and promoted osteogenic differentiation in the oxidative microenvironment. (**A**) Schematic diagram showing the effect of the HP-PVA@MH/Fe-Que on the hPDLSCs' osteogenic differentiation potential under oxidative stress conditions. (**B**) Cell morphology of hPDLSCs under oxidative stress condition. (**C**) ALP staining on day 7 and ARS staining on day 21 of hPDLSCs. (**D**) IF staining images of Runx2 and OCN in hPDLSCs

in Fig. S16A. To elucidate antioxidant properties in vivo, ROS was detected using a Multimodal Small Animal Live Imaging System. Following the establishment of the periodontitis model, the hydrogels were positioned between the upper first molar and second molar. One week later, a ROS fluorescent probe was injected into the periodontitis site. As shown in Fig. S16B, the periodontitis group exhibited elevated fluorescence signals, suggesting an accumulation of ROS in the periodontal tissue. The fluorescence signal in the HP-PVA group was slightly lower than that in the control group, suggesting that the hydrogel has ROS responsiveness and can remove part of the ROS. The fluorescence intensity of the HP-PVA@MH, HP-PVA@Fe-Que, and HP-PVA@MH/Fe-Que groups were significantly lower than that of the periodontitis group, and the fluorescence intensity of HP-PVA@MH/Fe-Que was the lowest. The statistical data in Fig. S16C confirmed the results, indicating that HP-PVA has partial ROS removal ability, and HP-PVA@MH/Fe-Que has excellent ROS removal ability in vivo. Furthermore, the ability of the HP-PVA@MH/Fe-Que hydrogels to scavenge ROS activity in RAW264.7 cells was tested in vitro. The results again showed that the HP-PVA@MH/Fe-Que hydrogels had a remarkable ROS scavenge efficiency (Fig. S16D, E).

Bone regeneration evaluation of the hydrogels in vivo

To evaluate the therapeutic effect of HP-PVA@MH/Fe-Que hydrogels on bone resorption in vivo, samples from the maxillary bone were obtained for analysis using Micro-CT at 2 weeks and 4 weeks following the hydrogel treatment (Fig. 9A). 2D and 3D images were used for visualization of the reconstruction of the alveolar bone, showing the destruction of the alveolar bone and resorption at the root divergence, reflecting the inflammatory process of the periodontal disease model. The extent of bone loss in the alveolar bone was quantified by measuring the linear distance from the distal cementoenamel junction (CEJ) of the first molar to the apex of the alveolar bone crest (ABC). As shown in Fig. 9B and C, the periodontitis group exhibited significant bone loss between the first and second molars, surpassing the diameter of the ligated elastic wire (0.2 mm). Furthermore, the alveolar bone resorption reached approximately one-third of the root length, confirming the successful establishment of the periodontitis model. The SD rats treated with HP-PVA, HP-PVA@MH, and HP-PVA@Fe-Que showed improved bone regeneration in the alveolar bone. Furthermore, the bone regeneration was more noticeable when treated with HP-PVA@MH/Fe-Que. Corresponding quantitative results are plotted in Fig. 9D-G. Among them, when evaluating the second week of the lateral alveolar bone defect, we found that the alveolar bone loss in the periodontitis group (1.51 ± 0.06 mm) was significantly increased compared with the control group (0.46 ± 0.02 mm). Compared with the periodontitis group, the rats treated with HP-PVA (1.39 ± 0.03 mm), HP-PVA@MH (1.24 ± 0.08 mm), and HP-PVA@Fe-Que (1.25 ± 0.05 mm) showed the reduction in alveolar bone loss, and the rats treated with HP-PVA@MH/Fe-Que (0.83 ± 0.06 mm) showed the best alveolar bone restoration. In the fourth week, the buccal lateral alveolar bone defect of control, periodontitis, HP-PVA, HP-PVA@MH, HP-PVA@Fe-Que, and HP-PVA@MH/Fe-Que groups were 0.37 ± 0.05, 1.42 ± 0.05, 1.04 ± 0.05, 0.72 ± 0.09, 0.70 ± 0.02 and 0.60 ± 0.02 mm. All other indicators showed that the alveolar bone partially recovered after HP-PVA@MH/Fe-Que hydrogels treatment, consistently confirming that HP-PVA@MH/Fe-Que saved the alveolar bone loss in inflammatory diseases and had good therapeutic effects on periodontitis in vivo.

Remodeling and regeneration of periodontal tissues in periodontitis in vivo

After verifying the restorative activity of HP-PVA@MH/Fe-Que through Micro-CT analysis, we conducted histological analysis to further validate the pathological changes in periodontal tissues. In the control group, epithelial attachment was normal at 2 weeks, no periodontal pockets were formed, inflammatory cell filtration was minimal, collagen fibers were well oriented, and shark teeth fibers were vertically inserted into the bone. In the periodontitis group, there was a loss of epithelial attachment in the gingiva, resorption of alveolar bone towards the root apex, extensive infiltration of inflammatory cells, and a disorganized arrangement of collagen fibers, all indicating significant inflammation within the periodontal tissue. In contrast, after treatment with HP-PVA@MH/Fe-Que, the junctional epithelial attachment was partially restored, inflammatory cell infiltration was reduced, and the ABC height was partially restored (Fig. S17A). The efficiency of periodontitis treatment was evaluated by Masson trichrome staining (the blue area represents collagen staining), which showed that the collagen deposition level was reduced in the periodontitis group, and the collagen fiber structure was disordered and irregular (Fig. S17B). After treatment with HP-PVA@MH/Fe-Que, the collagen fibers were more compact and ordered. These results can also be confirmed by the quantitative results of inflammatory cell and collagen content in Fig. S17D, E.

In 4 weeks, we observed limited bone loss recovery in the periodontitis group, with disordered connective tissue structure (Fig. 10A, B). In the HP-PVA treatment group, there was slight recovery of the connective tissue and alveolar bone height, with no significant effect on the treatment of periodontitis. The inflammatory cell infiltration was significantly less in the HP-PVA@Fe-Que and

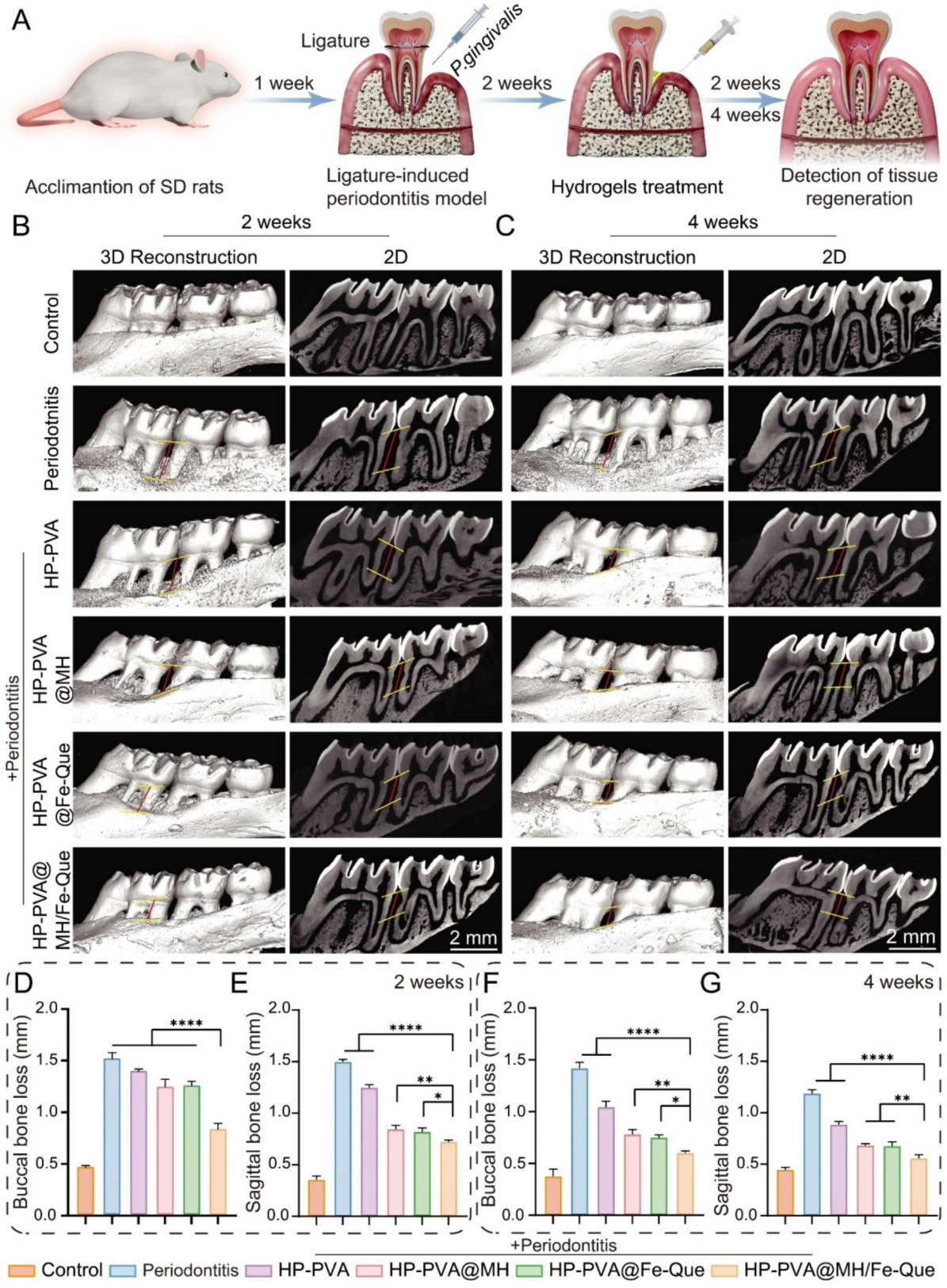

Fig. 9 HP-PVA@MH/Fe-Que hydrogels reduced alveolar bone loss in rat models of periodontitis. (**A**) Schematic illustration of the treatment procedure for the in vivo study. (**B**) 3D reconstruction, sagittal images of the alveolar bone in 2 weeks (upper dashed line: CEJ, lower dashed line: ABC, red line: bone loss). (**C**) Images in 3D reconstruction and 2D sagittal view taken four weeks post-implantation. (**D**) Assessment of the height of lateral buccal bone loss in quantitative terms and (**E**) sagittal bone loss of 2 weeks. (**F**) Quantitative evaluation lateral buccal bone loss height and (**G**) sagittal bone loss of 4 weeks

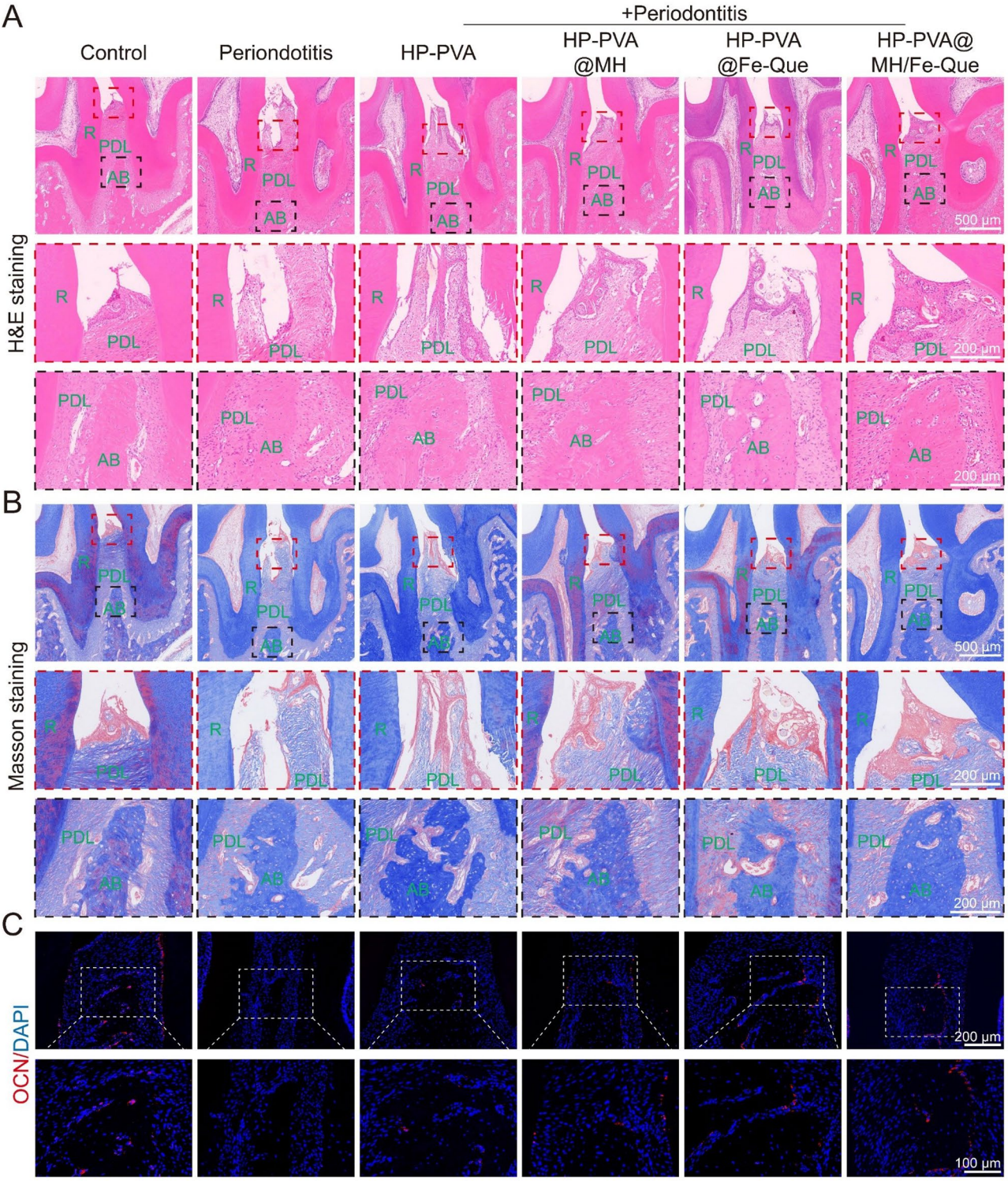

Fig. 10 HP-PVA@MH/Fe-Que hydrogels alleviated the imbalance of periodontal bone homeostasis in rat models of periodontitis after 4 weeks of treatment. (**A**) Images of H&E staining. (**B**) Masson's trichrome staining images of the alveolar bone. (**C**) IF staining of osteoinductive marker OCN in the alveolar bone. R: root, PDL: periodontal ligament, AB: alveolar bone

HP-PVA@MH groups than in the periodontitis group after treatment, and the alveolar bone heights were significantly restored. The HP-PVA@MH/Fe-Que group showed the best effect, with the gingiva, periodontal ligament, and alveolar bone structure approaching normal. These results can also be confirmed by the quantitative results of inflammatory cell and collagen content in Fig. S18A, B. These results collectively indicate that HP-PVA@MH/Fe-Que had a significant therapeutic effect on the bacteria-induced periodontitis model, reducing inflammatory responses in periodontal tissues and accelerating the recovery of periodontitis.

To verify the osteogenic activity of HP-PVA@MH/Fe-Que in the post-inflammatory tissue regeneration stage, Runx2 (2 weeks) and OCN (4 weeks) were used to verify the potential osteogenic expression during bone formation by IF staining (Fig. S17C, 10 C). The expression of Runx2 and OCN was downregulated in the periodontitis group, indicating that the ability to regenerate bone was reduced during periodontitis (Fig. S17F, S18C). Compared with the periodontitis group, the expression of Runx2 and OCN was upregulated after treatment with HP-PVA@MH/Fe-Que hydrogel, showing that HP-PVA@MH/Fe-Que hydrogel treatment had a positive regulatory effect on the restoration of periodontal bone tissue.

Anti-inflammatory effect of the hydrogels in vivo

HP-PVA@MH/Fe-Que exhibited protective effects against tissue damage; therefore, we explored their potential therapeutic mechanisms. We evaluated the levels of inflammation-related cytokines using immunohistochemistry (IHC) staining and IF staining in vivo. IHC staining showed that the positive staining areas for pro-inflammatory factors IL-1β and TNF-α were slightly lower in the HP-PVA group compared to the periodontitis group, and the positive staining areas were further reduced after treatment with HP-PVA@MH and HP-PVA@Fe-Que; while the lowest positive staining area was observed in the HP-PVA@MH/Fe-Que group (Fig. 11A, D, E). These results indicate that HP-PVA could scavenge part of the ROS and slightly alleviate inflammation due to its ROS responsiveness. After treatment with HP-PVA@MH and HP-PVA@Fe-Que, the inflammatory response was further reduced. However, due to the ROS-triggered release of antibacterial agent MH and anti-inflammatory nanoparticles Fe-Que NPs, HP-PVA@MH/Fe-Que eliminated the local bacteria in the periodontal pockets and inhibited inflammation, restoring periodontal tissue.

In periodontitis, M1 macrophages proliferate excessively and release various pro-inflammatory factors, further aggravating the inflammation. Next, we evaluated the immune-modulating function of the hydrogel. We performed IF staining of M1 and M2 macrophages with iNOS and CD206, respectively. Figure 11B showed that the fluorescence intensity of iNOS in the periodontitis group was the highest, indicating a significant increase in expression, while the expression of CD206 was lower. After treatment with HP-PVA@MH/Fe-Que hydrogel, the fluorescence intensity of M1 macrophages significantly decreased, while the fluorescence intensity of M2 macrophages significantly increased (Fig. 11F, G), indicating that the HP-PVA@MH/Fe-Que group can inhibit the polarization of M1 macrophages and promote the polarization of M2 macrophages, and with good immune modulating function.

Nrf2 can enhance the antioxidant stress resistance to reduce inflammatory responses by activating specific genes such as NF-κB in periodontitis [40]. Based on the previous LPS model results in vitro (Fig. 7A, B, I), we further explored the expression of Nrf2 and NF-κB in vivo. As shown in Fig. 11C, Nrf2 expression was low in the periodontitis group, while the Nrf2 protein level was higher in the HP-PVA@MH/Fe-Que group than in the periodontitis group (Fig. 11H). This result indicated that HP-PVA@MH/Fe-Que had better antioxidant capacity. Additionally, compared with the control group, the P65 protein level was higher in the periodontitis group, indicating that the NF-κB signaling pathway was activated. However, the P65 protein level was lower in the HP-PVA@MH/Fe-Que group than in the periodontitis group (Fig. 11I), indicating that HP-PVA@MH/Fe-Que had good potential to inhibit the NF-κB signaling pathway and reduce inflammation.

In summary, the HP-PVA@MH/Fe-Que hydrogel had a significant therapeutic effect on the bacteria-induced periodontitis model, which could scavenge ROS and alleviate oxidative stress in periodontal tissues. Secondly, it promoted the expression of Nrf2 and inhibited the expression of P65, regulating the Nrf2/NF-κB pathway to achieve immune modulation, inhibiting the polarization of M1 macrophages and promoting the polarization of M2 macrophages, thereby alleviating the inflammatory response in periodontal tissues. Furthermore, the expression of anti-inflammatory factors and bone-forming genes was also upregulated. All these factors work together to create an immune microenvironment favorable for the resolution of periodontitis and the regeneration of periodontal tissues.

Conclusion

In this study, we successfully designed a ROS-responsive hydrogel that can efficiently load antibacterial agents and anti-inflammatory nanoparticles to treat periodontitis. The HP-PVA@MH/Fe-Que hydrogel has excellent physical properties and can be used for local drug delivery in irregular periodontal pockets characterized by a high ROS microenvironment. The in vitro experimental

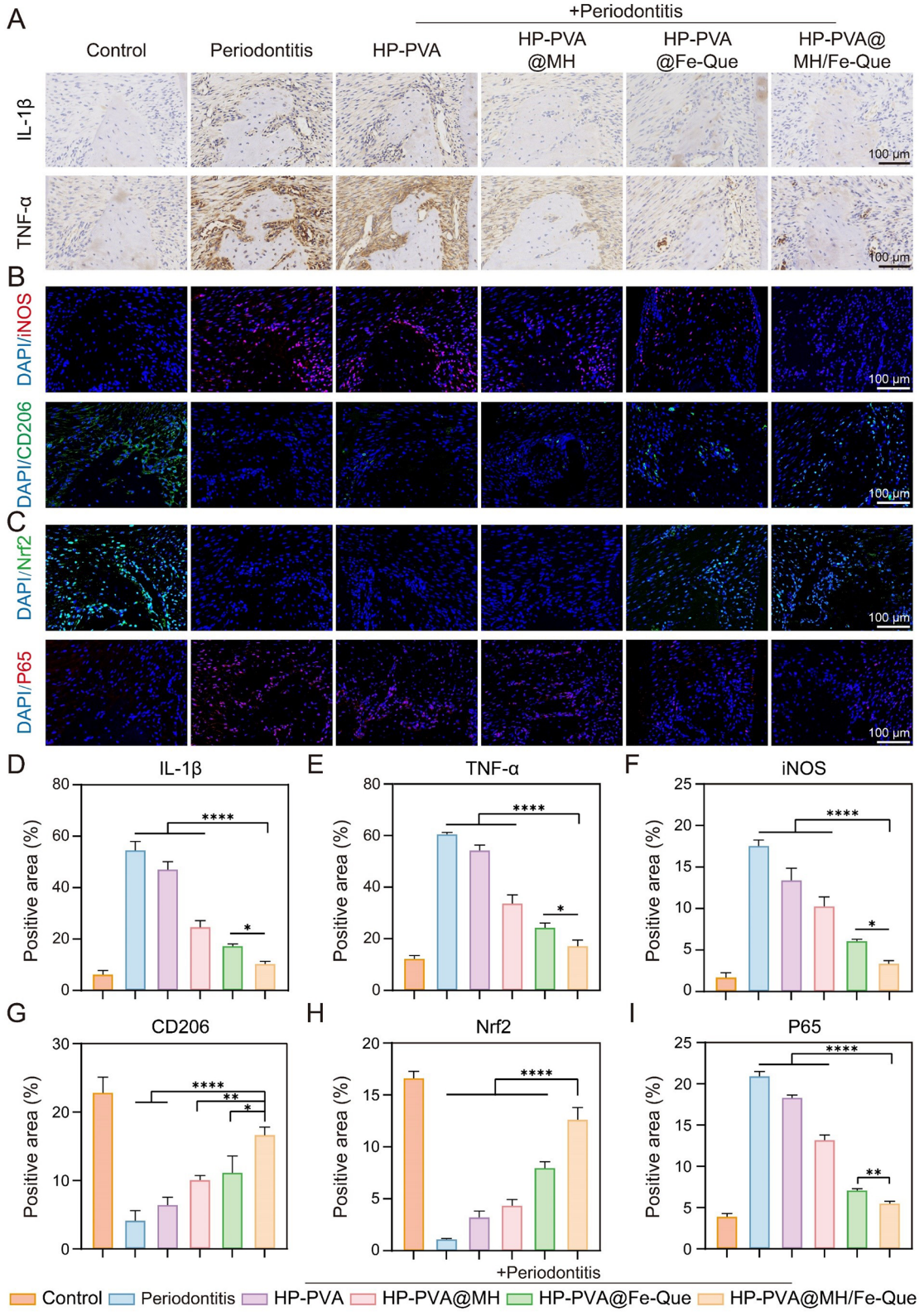

Fig. 11 HP-PVA@MH/Fe-Que hydrogels relieved periodontal tissue inflammation in rat models of periodontitis. (**A**) Representative IHC staining images of periodontal tissues, including *IL-1β* and *TNF-α*. (**B**) Immunofluorescence staining images of iNOS and CD206 in the area of the alveolar septal region. (**C**) Immunofluorescence staining images of Nrf2 and P65 in the region of the alveolar septum. (**D**-**I**) The corresponding quantitative analysis of IL-1β, TNF-α, iNOS, CD206, Nrf2, and P65

results show that HP-PVA@MH/Fe-Que has strong antibacterial effects, excellent ROS scavenging, and can regulate the Nrf2/NF-κB pathway to polarize macrophages, inhibit pro-inflammatory factor expression, promote anti-inflammatory factor and antioxidant enzyme expression, and ultimately save hPDLSCs from osteogenic differentiation under oxidative stress conditions. In an animal model of periodontitis in rats, the HP-PVA@MH/Fe-Que hydrogel can effectively remove ROS, alleviate inflammation, restore periodontal homeostasis, and promote the repair of alveolar bone defects. Therefore, this strategy of responding to the high ROS level microenvironment to trigger drug release and facilitate the synergistic delivery of antibacterial agents alongside anti-inflammatory nanoparticles holds significant promise for treating periodontitis and enhancing the regeneration of periodontal tissues.

Supplementary Information

The online version contains supplementary material available at https://doi.org/10.1186/s12951-025-03275-4.

Supplementary Material 1

Author contributions

YZ: Conceptualization, Methodology, Data curation, Writing-Original Draft. ZX: Formal analysis, Experiment, Methodology. XJ: Formal analysis, Investigation, Experiment, Methodology, Visualization. HZ: Investigation, Software, Visualization. XL: Software, Validation, Visualization. YF: Validation, Visualization. BL: Software, Validation. RC, CL and GT: Conceptualization, Project administration, Writing-Review & Editing, Funding acquisition. All authors reviewed the manuscript.

Funding

This work was funded by Sichuan Science and Technology Program (2024NSFSC1655, 2022YFS0634), Luzhou Science and Technology Program (2024JYJ035, 2023SYF101), Sichuan Province Medical Youth Innovation Research Project (Q23010), Scientific Research Foundation of Southwest Medical University (2023ZD002), Project of Stomatological Institute of Southwest Medical University (2021XJYJS01), Scientific Research Foundation of the Affiliated Stomatological Hospital of Southwest Medical University (2024KQZX04, 2023BS01, 2023KQ03, 2023Z01).

Data availability

No datasets were generated or analysed during the current study.

Declarations

Ethics approval and consent to participate

All animal experiments were approved by the animal ethics committee of Southwest Medical University (Document No. 20230705-005).

Consent for publication

All authors agree for publication.

Competing interests

The authors declare no competing interests.

Author details

[1]Oral & Maxillofacial Reconstruction and Regeneration of Luzhou Key Laboratory, The Affiliated Stomatological Hospital, Southwest Medical University, Luzhou 646000, China
[2]Department of Periodontics & Oral Mucosal Diseases, The Affiliated Stomatological Hospital, Southwest Medical University, Luzhou 646000, China
[3]Department of Periodontics & Oral Mucosal Diseases, Deyang Stomatological Hospital, Deyang 618000, China
[4]Institute of Stomatology, Southwest Medical University, Luzhou 646000, China

Received: 29 November 2024 / Accepted: 24 February 2025
Published online: 12 March 2025

References

1. Armitage GC. Periodontal diagnoses and classification of periodontal diseases. Periodontol 2000. 2004;34:9–21. https://doi.org/10.1046/j.0906-6713.2002.003421.x.
2. Williams DW, Greenwell-Wild T, Brenchley L, Dutzan N, Overmiller A, Sawaya AP, Webb S, Martin D, Genomics NN, Computational Biology C, et al. Human oral mucosa cell atlas reveals a stromal-neutrophil axis regulating tissue immunity. Cell. 2021;184:4090–e41044015. https://doi.org/10.1016/j.cell.2021.05.013.
3. Kinane DF, Stathopoulou PG, Papapanou PN. Periodontal diseases. Nat Rev Dis Primers. 2017;3:17038. https://doi.org/10.1038/nrdp.2017.38.
4. Tonetti MS, Chapple ILC. Biological approaches to the development of novel periodontal therapies– Consensus of the seventh European workshop on periodontology. J Clin Periodontol. 2011;38:114–8. https://doi.org/10.1111/j.1600-051X.2010.01675.x.
5. Hathaway-Schrader JD, Novince CM. Maintaining homeostatic control of periodontal bone tissue. Periodontol. 2000. 2021;86:157–187. https://doi.org/10.1111/prd.12368
6. Feng Z, Weinberg A. Role of bacteria in health and disease of periodontal tissues. Periodontol. 2000. 2006;40:50–76. https://doi.org/10.1111/j.1600-0757.2005.00148.x
7. Yin Y, Yang S, Ai D, Qin H, Sun Y, Xia X, Xu X, Ji W, Song J. Rational design of bioactive hydrogels toward periodontal delivery: from pathophysiology to therapeutic applications. Adv Funct Mater. 2023;33:2301062. https://doi.org/10.1002/adfm.202301062.
8. Zhao X, Yang Y, Yu J, Ding R, Pei D, Zhang Y, He G, Cheng Y, Li A. Injectable hydrogels with high drug loading through B-N coordination and ROS-triggered drug release for efficient treatment of chronic periodontitis in diabetic rats. Biomaterials. 2022;282:121387. https://doi.org/10.1016/j.biomaterials.2022.121387.
9. Pan S, Zhong W, Lan Y, Yu S, Yang L, Yang F, Li J, Gao X, Song J. Pathology-Guided cell Membrane-Coated polydopamine nanoparticles for efficient multisynergistic treatment of periodontitis. Adv Funct Mater. 2024;34:202312253. https://doi.org/10.1002/adfm.202312253.
10. Yang S, Zhu Y, Ji C, Zhu H, Lao A, Zhao R, Hu Y, Zhou Y, Zhou J, Lin K, Xu Y. A five-in-one novel MOF-modified injectable hydrogel with thermo-sensitive and adhesive properties for promoting alveolar bone repair in periodontitis: antibacterial, hemostasis, immune reprogramming, pro-osteo-/angiogenesis and recruitment. Bioact Mater. 2024;41:239–56. https://doi.org/10.1016/j.bioactmat.2024.07.016.
11. Dong Z, Lin Y, Xu S, Chang L, Zhao X, Mei X, Gao X. NIR-triggered tea polyphenol-modified gold nanoparticles-loaded hydrogel treats periodontitis by inhibiting bacteria and inducing bone regeneration. Mater Design. 2023;225:111487. https://doi.org/10.1016/j.matdes.2022.111487.
12. Wang P, Wang L, Zhan Y, Liu Y, Chen Z, Xu J, Guo J, Luo J, Wei J, Tong F, Li Z. Versatile hybrid nanoplatforms for treating periodontitis with chemical/photothermal therapy and reactive oxygen species scavenging. Chem Eng J. 2023;463:142293. https://doi.org/10.1016/j.cej.2023.142293.
13. Wang L, Li Y, Ren M, Wang X, Li L, Liu F, Lan Y, Yang S, Song J. pH and lipase-responsive nanocarrier-mediated dual drug delivery system to treat periodontitis in diabetic rats. Bioactive Mater. 2022;18:254–66. https://doi.org/10.1016/j.bioactmat.2022.02.008.
14. Lou J, Mooney DJ. Chemical strategies to engineer hydrogels for cell culture. Nat Reviews Chem. 2022;6:726–44. https://doi.org/10.1038/s41570-022-00420-7.
15. Ye B, Xiang R, Luo F. Hydrogel-Based drug delivery systems for diabetes bone defects. Chem Eng J. 2024;497:154436. https://doi.org/10.1016/j.cej.2024.154436.

16. Huang M, Huang Y, Liu H, Tang Z, Chen Y, Huang Z, Xu S, Du J, Jia B. Hydrogels for the treatment of oral and maxillofacial diseases: current research, challenges, and future directions. Biomater Sci. 2022;10:6413–46. https://doi.org/10.1039/d2bm01036d.
17. Gan Z, Xiao Z, Zhang Z, Li Y, Liu C, Chen X, Liu Y, Wu D, Liu C, Shuai X, Cao Y. Stiffness-tuned and ROS-sensitive hydrogel incorporating complement C5a receptor antagonist modulates antibacterial activity of macrophages for periodontitis treatment. Bioact Mater. 2023;25:347–59. https://doi.org/10.1016/j.bioactmat.2023.01.011.
18. Wu Y, Wang Y, Long L, Hu C, Kong Q, Wang Y. A Spatiotemporal release platform based on pH/ROS stimuli-responsive hydrogel in wound repairing. J Control Release. 2022;341:147–65. https://doi.org/10.1016/j.jconrel.2021.11.027.
19. Zhang L, Bei Z, Li T, Qian Z. An injectable conductive hydrogel with dual responsive release of Rosmarinic acid improves cardiac function and promotes repair after myocardial infarction. Bioact Mater. 2023;29:132–50. https://doi.org/10.1016/j.bioactmat.2023.07.007.
20. Ming P, Liu Y, Yu P, Jiang X, Yuan L, Cai S, Rao P, Cai R, Lan X, Tao G, Xiao J. A biomimetic Se-nHA/PC composite microsphere with synergistic Immunomodulatory and osteogenic ability to activate bone regeneration in periodontitis. Small. 2024;20:e2305490. https://doi.org/10.1002/smll.202305490.
21. Bai X, Peng W, Tang Y, Wang Z, Guo J, Song F, Yang H, Huang C. An NIR-propelled janus nanomotor with enhanced ROS-scavenging, Immunomodulating and biofilm-eradicating capacity for periodontitis treatment. Bioact Mater. 2024;41:271–92. https://doi.org/10.1016/j.bioactmat.2024.07.014.
22. Peng S, Fu H, Li R, Li H, Wang S, Li B, Sun J. A new direction in periodontitis treatment: biomaterial-mediated macrophage immunotherapy. J Nanobiotechnol. 2024;22:359. https://doi.org/10.1186/s12951-024-02592-4.
23. Liu X, Wan X, Sui B, Hu Q, Liu Z, Ding T, Zhao J, Chen Y, Wang ZL, Li L. Piezoelectric hydrogel for treatment of periodontitis through bioenergetic activation. Bioact Mater. 2024;35:346–61. https://doi.org/10.1016/j.bioactmat.2024.02.011.
24. He Z, Liu Y, Zheng ZL, Lv JC, Liu SB, Zhang J, Liu HH, Xu JZ, Li ZM, Luo E. Periodic Lamellae-Based nanofibers for precise Immunomodulation to treat inflammatory bone loss in periodontitis. Adv Healthc Mater. 2024;13:e2303549. https://doi.org/10.1002/adhm.202303549.
25. Cai G, Ren L, Yu J, Jiang S, Liu G, Wu S, Cheng B, Li W, Xia J. A Microenvironment-Responsive, controlled release hydrogel delivering Embelin to promote bone repair of periodontitis via Anti-Infection and Osteo-Immune modulation. Adv Sci. 2024;11:e202403786. https://doi.org/10.1002/advs.202403786.
26. Yang S, Yin Y, Sun Y, Ai D, Xia X, Xu X, Song J. AZGP1 aggravates macrophage M1 polarization and pyroptosis in periodontitis. J Dent Res. 2024;103:631–41. https://doi.org/10.1177/00220345241235616.
27. Li J, Wang Y, Tang M, Zhang C, Fei Y, Li M, Li M, Gui S, Guo J. New insights into nanotherapeutics for periodontitis: a triple concerto of antimicrobial activity, Immunomodulation and periodontium regeneration. J Nanobiotechnol. 2024;22:19. https://doi.org/10.1186/s12951-023-02261-y.
28. Lei M, Wan H, Song J, Lu Y, Chang R, Wang H, Zhou H, Zhang X, Liu C, Qu X. Programmable Electro-Assembly of collagen: constructing porous Janus films with customized dual signals for Immunomodulation and tissue regeneration in periodontitis treatment. Adv Sci (Weinh). 2024;11:e2305756. https://doi.org/10.1002/advs.202305756.
29. Xie Y, Xiao S, Huang L, Guo J, Bai M, Gao Y, Zhou H, Qiu L, Cheng C, Han X. Cascade and ultrafast artificial antioxidases alleviate inflammation and bone resorption in periodontitis. ACS Nano. 2023;17:15097–112. https://doi.org/10.1021/acsnano.3c04328.
30. Xin X, Liu J, Liu X, Xin Y, Hou Y, Xiang X, Deng Y, Yang B, Yu W. Melatonin-Derived carbon Dots with free radical scavenging property for effective periodontitis treatment via the Nrf2/HO-1 pathway. ACS Nano. 2024;18:8307–24. https://doi.org/10.1021/acsnano.3c12580.
31. Yang GG, Zhou DJ, Pan ZY, Yang J, Zhang DY, Cao Q, Ji LN, Mao ZW. Multifunctional low-temperature photothermal nanodrug with in vivo clearance, ROS-Scavenging and anti-inflammatory abilities. Biomaterials. 2019;216:119280. https://doi.org/10.1016/j.biomaterials.2019.119280.
32. Yang SY, Hu Y, Zhao R, Zhou YN, Zhuang Y, Zhu Y, Ge XL, Lu TW, Lin KL, Xu YJ. Quercetin-loaded mesoporous nano-delivery system remodels osteoimmune microenvironment to regenerate alveolar bone in periodontitis via the miR-21a-5p/PDCD4/NF-kappaB pathway. J Nanobiotechnol. 2024;22:94. https://doi.org/10.1186/s12951-024-02352-4.
33. Wang Y, Li C, Wan Y, Qi M, Chen Q, Sun Y, Sun X, Fang J, Fu L, Xu L, et al. Quercetin-Loaded ceria nanocomposite potentiate Dual-Directional immunoregulation via macrophage polarization against periodontal inflammation. Small. 2021;17:e2101505. https://doi.org/10.1002/smll.202101505.
34. Zhu H, Cai C, Yu Y, Zhou Y, Yang S, Hu Y, Zhu Y, Zhou J, Zhao J, Ma H, et al. Quercetin-Loaded bioglass injectable hydrogel promotes m6A alteration of Per1 to alleviate oxidative stress for periodontal bone defects. Adv Sci (Weinh). 2024;11:e2403412. https://doi.org/10.1002/advs.202403412.
35. Li Y, Li J, Chang Y, Zhang J, Wang Z, Wang F, Lin Y, Sui L. Mitochondria-targeted drug delivery system based on tetrahedral framework nucleic acids for bone regeneration under oxidative stress. Chem Eng J. 2024;496:153723. https://doi.org/10.1016/j.cej.2024.153723.
36. Gui S, Tang W, Huang Z, Wang X, Gui S, Gao X, Xiao D, Tao L, Jiang Z, Wang X. Ultrasmall coordination polymer nanodots Fe-Quer nanozymes for preventing and delaying the development and progression of diabetic retinopathy. Adv Funct Mater. 2023;33:2300261. https://doi.org/10.1002/adfm.202300261.
37. Han Z, Gao X, Wang Y, Cheng S, Zhong X, Xu Y, Zhou X, Zhang Z, Liu Z, Cheng L. Ultrasmall iron-quercetin metal natural product nanocomplex with antioxidant and macrophage regulation in rheumatoid arthritis. Acta Pharm Sin B. 2023;13:1726–39. https://doi.org/10.1016/j.apsb.2022.11.020.
38. Xu Y, Luo Y, Weng Z, Xu H, Zhang W, Li Q, Liu H, Liu L, Wang Y, Liu X, et al. Microenvironment-Responsive Metal-Phenolic nanozyme release platform with antibacterial, ROS scavenging, and osteogenesis for periodontitis. ACS Nano. 2023;17:18732–46. https://doi.org/10.1021/acsnano.3c01940.
39. Zhu S, Zhao B, Li M, Wang H, Zhu J, Li Q, Gao H, Feng Q, Cao X. Microenvironment responsive nanocomposite hydrogel with NIR photothermal therapy, vascularization and anti-inflammation for diabetic infected wound healing. Bioact Mater. 2023;26:306–20. https://doi.org/10.1016/j.bioactmat.2023.03.005.
40. Tian Y, Li Y, Liu J, Lin Y, Jiao J, Chen B, Wang W, Wu S, Li C. Photothermal therapy with regulated Nrf2/NF-kappaB signaling pathway for treating bacteria-induced periodontitis. Bioact Mater. 2022;9:428–45. https://doi.org/10.1016/j.bioactmat.2021.07.033.
41. Boda SK, Fischer NG, Ye Z, Aparicio C. Dual oral tissue adhesive nanofiber membranes for pH-Responsive delivery of antimicrobial peptides. Biomacromolecules. 2020;21:4945–61. https://doi.org/10.1021/acs.biomac.0c01163.
42. Qiao B, Wang J, Qiao L, Maleki A, Liang Y, Guo B. ROS-responsive hydrogels with Spatiotemporally sequential delivery of antibacterial and anti-inflammatory drugs for the repair of MRSA-infected wounds. Regenerative Biomaterials. 2023;11:rbad110. https://doi.org/10.1093/rb/rbad110.
43. Luo Q, Yang Y, Ho C, Li Z, Chiu W, Li A, Dai Y, Li W, Zhang X. Dynamic hydrogel-metal-organic framework system promotes bone regeneration in periodontitis through controlled drug delivery. J Nanobiotechnol. 2024;22:287. https://doi.org/10.1186/s12951-024-02555-9.
44. Wu Y, Wang Y, Long L, Hu C, Kong Q, Wang Y. A Spatiotemporal release platform based on pH/ROS stimuli-responsive hydrogel in wound repairing. J Controlled Release. 2022;341:147–65. https://doi.org/10.1016/j.jconrel.2021.11.027.
45. Qiao B, Wang J, Qiao L, Maleki A, Liang Y, Guo B. ROS-responsive hydrogels with Spatiotemporally sequential delivery of antibacterial and anti-inflammatory drugs for the repair of MRSA-infected wounds. Regenerative Biomaterials. 2024;11. https://doi.org/10.1093/rb/rbad110.
46. Dong Z, Sun Y, Chen Y, Liu Y, Tang C, Qu X. Injectable adhesive hydrogel through a microcapsule Cross-Link for periodontitis treatment. ACS Appl Bio Mater. 2019;2:5985–94. https://doi.org/10.1021/acsabm.9b00912.
47. Guo H, Huang S, Yang X, Wu J, Kirk TB, Xu J, Xu A, Xue W. Injectable and Self-Healing hydrogels with Double-Dynamic bond tunable mechanical, Gel-Sol transition and drug delivery properties for promoting periodontium regeneration in periodontitis. ACS Appl Mater Interfaces. 2021;13:61638–52. https://doi.org/10.1021/acsami.1c18701.
48. Zhang C, Yan R, Bai M, Sun Y, Han X, Cheng C, Ye L. Pt-Clusters-Equipped Antioxidase-Like biocatalysts as efficient ROS scavengers for treating periodontitis. Small. 2024;20:e2306966. https://doi.org/10.1002/smll.202306966.
49. Wang Y, Yuan Y, Wang R, Wang T, Guo F, Bian Y, Wang T, Ma Q, Yuan H, Du Y, et al. Injectable thermosensitive gel CH-BPNs-NBP for effective periodontitis treatment through ROS-Scavenging and jaw vascular unit protection. Adv Healthc Mater. 2024;13:e2400533. https://doi.org/10.1002/adhm.202400533.
50. Liu Y, Yan J, Chen L, Liao Y, Huang L, Tan J. Multifunctionalized and Dual-Crosslinked hydrogel promotes inflammation resolution and bone regeneration via NLRP3 Inhibition in periodontitis. Small Struct. 2024;5. https://doi.org/10.1002/sstr.202300281.
51. Gong J, Wang S, Liu J, Zhang Y, Li J, Yang H, Liang K, Deng Y. In situ oxygen-generating bio-heterojunctions for enhanced anti-bacterial treatment of

anaerobe-induced periodontitis. Chem Eng J. 2024;498. https://doi.org/10.1016/j.cej.2024.155083.
52. Xia P, Yu M, Yu M, Chen D, Yin J. Bacteria-responsive, Cell-recruitable, and osteoinductive nanocomposite microcarriers for intelligent bacteriostasis and accelerated tissue regeneration. Chem Eng J. 2023;465:142972. https://doi.org/10.1016/j.cej.2023.142972.
53. Thananukul K, Kaewsaneha C, Opaprakasit P, Lebaz N, Errachid A, Elaissari A. Smart gating porous particles as new carriers for drug delivery. Adv Drug Deliv Rev. 2021;174:425–46. https://doi.org/10.1016/j.addr.2021.04.023.
54. Zhu B, Wu J, Li T, Liu S, Guo J, Yu Y, Qiu X, Zhao Y, Peng H, Zhang J, et al. A glutathione Peroxidase-Mimicking nanozyme precisely alleviates reactive oxygen species and promotes periodontal bone regeneration. Adv Healthc Mater. 2024;13:e2302485. https://doi.org/10.1002/adhm.202302485.
55. Guo J, Xing Z, Liu L, Sun Y, Zhou H, Bai M, Liu X, Adeli M, Cheng C, Han X. Antioxidase-Like nanobiocatalysts with ultrafast and reversible Redox-Centers to secure stem cells and periodontal tissues. Adv Funct Mater. 2023;33:202211778. https://doi.org/10.1002/adfm.202211778.
56. Xu Z, Zhu Y, Xie M, Liu K, Cai L, Wang H, Li D, Chen H, Gao L. Mackinawite nanozymes as reactive oxygen species scavengers for acute kidney injury alleviation. J Nanobiotechnol. 2023;21:281. https://doi.org/10.1186/s12951-023-02034-7.
57. Zhang Y, Zhang H, Zhao F, Jiang Z, Cui Y, Ou M, Mei L, Wang Q. Mitochondrial-targeted and ROS-responsive nanocarrier via nose-to-brain pathway for ischemic stroke treatment. Acta Pharm Sin B. 2023;13:5107–20. https://doi.org/10.1016/j.apsb.2023.06.011.
58. Hu S, Wang L, Li J, Li D, Zeng H, Chen T, Li L, Xiang X. Catechol-Modified and MnO(2)-Nanozyme-Reinforced hydrogel with improved antioxidant and antibacterial capacity for periodontitis treatment. ACS Biomater Sci Eng. 2023;9:5332–46. https://doi.org/10.1021/acsbiomaterials.3c00454.
59. Tian M, Chen G, Xu J, Lin Y, Yi Z, Chen X, Li X, Chen S. Epigallocatechin gallate-based nanoparticles with reactive oxygen species scavenging property for effective chronic periodontitis treatment. Chem Eng J. 2022;433:132197. https://doi.org/10.1016/j.cej.2021.132197.
60. Liu X, Hou Y, Yang M, Xin X, Deng Y, Fu R, Xiang X, Cao N, Liu X, Yu W, et al. N-Acetyl-l-cysteine-Derived carbonized polymer Dots with ROS scavenging via Keap1-Nrf2 pathway regulate alveolar bone homeostasis in periodontitis. Adv Healthc Mater. 2023;12:e2300890. https://doi.org/10.1002/adhm.202300890.
61. Yang G, Fan M, Zhu J, Ling C, Wu L, Zhang X, Zhang M, Li J, Yao Q, Gu Z, Cai X. A multifunctional anti-inflammatory drug that can specifically target activated macrophages, massively deplete intracellular H(2)O(2), and produce large amounts CO for a highly efficient treatment of osteoarthritis. Biomaterials. 2020;255:120155. https://doi.org/10.1016/j.biomaterials.2020.120155.
62. Liu S, Wang W, Wu P, Chen Z, Pu W, Li L, Li G, Zhang J, Song J. Pathogenesis-Guided engineering of Multi-Bioactive hydrogel Co-Delivering Inflammation-Resolving nanotherapy and Pro-Osteogenic protein for bone regeneration. Adv Funct Mater. 2023;33:2301523. https://doi.org/10.1002/adfm.202301523.
63. Sun H, Xu J, Wang Y, Shen S, Xu X, Zhang L, Jiang Q. Bone microenvironment regulative hydrogels with ROS scavenging and prolonged oxygen-generating for enhancing bone repair. Bioact Mater. 2023;24:477–96. https://doi.org/10.1016/j.bioactmat.2022.12.021.
64. Wang H, Zhang Y, Zhang Y, Li C, Zhang M, Wang J, Zhang Y, Du Y, Cui W, Chen W. Activating macrophage continual efferocytosis via microenvironment biomimetic short fibers for reversing inflammation in bone repair. Adv Mater. 2024;36:e2402968. https://doi.org/10.1002/adma.202402968.
65. Bai L, Feng M, Li Q, Zhao Y, Zhang G, Cai Z, Xiao J, Lin Y. Curcumin delivery using tetrahedral framework nucleic acids enhances bone regeneration in osteoporotic rats. Chem Eng J. 2023;472:144978. https://doi.org/10.1016/j.cej.2023.144978.
66. Dos Santos DM, Moon JI, Kim DS, Bassous NJ, Marangon CA, Campana-Filho SP, Correa DS, Kang MH, Kim WJ, Shin SR. Hierarchical Chitin Nanocrystal-Based 3D printed dual-Layer membranes hydrogels: A dual drug delivery Nano-Platform for periodontal tissue regeneration. ACS Nano. 2024;18:24182–203. https://doi.org/10.1021/acsnano.4c05558.

Publisher's note